Novel direct injection electro-hydraulic model-based controller for high efficiency internal combustion engines

NOVEL DIRECT INJECTION ELECTRO-HYDRAULIC MODEL-BASED CONTROLLER FOR HIGH EFFICIENCY INTERNAL COMBUSTION ENGINES

Pier Paolo Brancaleoni, Davide Viscione, Giacomo Silvagni, Vittorio Ravaglioli, Enrico Corti, Gian Marco Bianchi

DIN – Dipartimento di Ingegneria Industriale, Alma Mater Studiorum – Università di Bologna, Bologna, 40121 Italy

pier.brancaleoni2@unibo.it; davide.viscione2@unibo.it; giacomo.silvagni2@unibo.it; vittorio.ravaglioli2@unibo.it; enrico.corti2@unibo.it; gianmarco.bianchi@unibo.it

Matteo De Cesare, Federico Stola

Marelli Europe S.p.A.

Matteo.Decesare@marelli.com; Federico.Stola@marelli.com;

CORRESPONDING AUTHOR

Pier Paolo Brancaleoni, pier.brancaleoni2@unibo.it, DIN – Dipartimento di Ingegneria Industriale, Alma Mater Studiorum – Università di Bologna, Bologna, 40121 Italy

ABSTRACT

During the past years, automotive industries developed several technologies suitable to increase efficiency and reduce emissions from Internal Combustion Engines (ICEs). Among them, the adoption of high-pressure injection systems is considered crucial to optimize air-fuel mixture formation. However, the use of these technologies also promotes the formation of particulate matter (PM), which is a direct result of charge stratification and fluid film on the cylinder walls. Therefore, to obtain a proper mixture formation without the risk of wall impingement, the utilization of consecutive injections is mandatory. Since modern Gasoline Direct Injection (GDI) systems are typically characterized by electrical-actuated injectors connected to a single high-pressure rail, a deep understanding of electrical and hydraulic effects among two close injection events becomes essential. This paper analyzes the combinations of electrical and hydraulic effects that occur in a high-pressure GDI system performing multiple injections. By using a specifically developed open vessel flushing bench, the injection system has been characterized in terms of pressure wave propagation as well as electrical distortions of the driving current profile of the injectors. The analysis of the experimental data has allowed for the calibration of the residual magnetization characteristic map in addition to the development of a pressure wave propagation control-oriented model. Finally, a Magnetization and Pressure Wave (MPW) correction strategy, easily implementable on an Electronic Control Unit (ECU) without the need for additional sensors, has been proposed. By running the MPW strategy, the error between the actual and expected injected mass has been reduced below 5% in all tested conditions.

KEYWORDS

- GDI System
- Multiple Injections
- Residual Magnetization

- Pressure Fluctuations
- Injected Fuel Mass Variation
- Control-Oriented Modelling

SYMBOLS/ABBREVIATIONS

$\mathbf{A_1}$	Electric charge on the injection coil in magnetized conditions
$\mathbf{A_2}$	Electric charge on the injection coil in unmagnetized conditions
BEV	Battery Electric Vehicle
$\mathbf{A_3}$	Difference between magnetized and unmagnetized electric charge
CCV	Cycle-to-Cycle Variability
CR	Common Rail
DI	Direct Injection
DoF	Degree of Freedom
DT	Dwell Time
dt	Time differential
ECU	Electronic Control Unit
EOI	End Of Injection
$\mathbf{ET}_{corrected}$	Corrected Energizing Time to compensate the magnetization phenomenon
$\mathbf{ET}_{eq}$	Equivalent Energizing Time due to the magnetization phenomenon
$\mathbf{ET_1}$	Energizing Time of the first injection pulse
$\mathbf{ET_2}$	Energizing Time of the second injection pulse
$\mathbf{ET}_{2corr}$	Energizing Time correction of magnetization effect
$\mathbf{ET}_{2Final}$	Energizing Time correction of magnetization and wave effects
$\mathbf{ET}_{2w}$	Energizing Time correction of wave effect
FEV	Fuel Cell Electric Vehicle
GCI	Gasoline Compression Ignition
GDI	Gasoline Direct Injection
GPF	Gasoline Particulate Filter
HEV	Hybrid Electric Vehicle
HP	High Pressure
i(t)	Current behavior in time
ICE	Internal Combustion Engine
LP	Low Pressure
LTC	Low Temperature Combustion
$\mathbf{m_1}$	Target mass for fist injection
$\mathbf{m_2}$	Target mass for second injection
MPROP	Magnetic Proportional
MPW	Magnetization and Pressure Wave Correction Strategy
MSD	Mass Spring Damper
PFI	Port Fuel Injection
PKistInj	Pressure from Kistler Sensor mounted on feed duct Injector Side
PKistRail	Pressure from Kistler sensor mounted on feed duct Rail Side
PM	Particulate Matter
PRail	Rail Pressure Signal
PWM	Pulse Width Modulation
Q	Electric charge on the injector coil
RCP	Rapid Control Prototyping
RM	Residual Magnetization
RMSE	Root Mean Squared Error

RON	Research Octane Number
RPM	Revolution Per Minute
SA	Spark Advance
SACI	Spark Assisted Compression Ignition
SNR	Signal to Noise Ratio
SOI	Start Of Injection
TWC	Three Way Catalyst
UHC	Unburnt Hydrocarbon
ΔET	Variation of Energizing Time due to the magnetization phenomenon
$\boldsymbol{c}$	Equivalent Damping
$\boldsymbol{\xi}$	Damping Ratio
$\boldsymbol{k}$	Equivalent Stiffness
$\boldsymbol{m}$	Equivalent Inertia
$\boldsymbol{\omega_d}$	Damped Natural Frequency
$\boldsymbol{\omega_n}$	Natural Frequency
$\boldsymbol{v_0}$	Initial Condition
$\boldsymbol{x_0}$	Initial Condition

INTRODUCTION

Over the past years, to develop increasingly efficient powertrains, many solutions have been proposed. Among these, hybrid vehicles, which normally involve the combined use of an Internal Combustion Engine (ICE) and an electric motor, are often a good compromise solution, mainly because of the current technological limitations of Battery Electric Vehicles (BEVs), such as long charging time and limited rangeability [1-2]. In this scenario, the development of less polluting and more efficient engines remains crucial to ensure optimal utilization of energy resources during the current and future energy transition. Many authors [3-6] demonstrated the potential of HEVs based on modern Spark Ignited (SI) ICEs, usually equipped with a high-pressure Gasoline Direct Injection (GDI) system. The adoption of a GDI system allows injecting gasoline at high pressure directly into the combustion chamber. This system results beneficial to improve combustion efficiency, phasing, duration and injected fuel quantity [7,8]. Conversely, Liang et al. [9] demonstrated that GDI engines are characterized by high Particulate Matter and Unburned Hydrocarbon (UHC) emission. As explained by Catapano et al. [10], high PM production is typically related to an incomplete vaporization of some fuel droplets. Moreover, other works in the literature [11] report that the high protrusion capability of the fuel jet might increase the PM production due to the formation of a thin gasoline film on the cylinder walls. Therefore, to mitigate engine-out emissions in GDI engines, complex aftertreatment systems [12], typically composed of the Three-Way-Catalyst (TWC) and Gasoline Particulate Filter (GPF), have been adopted. Unfortunately, the backpressure increase produced by the GPF raises the pumping work and knock tendency, affecting the overall engine efficiency. A possible approach to mitigate PM production is strictly connected to the injection strategy management (increasing the injection pressure and optimizing the Start of Injection (SOI) [13]). Yamaguchi et al. [14] demonstrated that a higher injection pressure results beneficial to obtain smaller fuel droplets, thus shortening the vaporization process. On the other hand, the fuel jet's protrusion is directly related to the injection pressure: the higher the injection pressure, the longer the penetration promoting the cylinder wall impingement. The adoption of a multiple injection strategy is crucial to overcome this limitation and maximize the benefits of high-pressure GDI systems. Injecting the required fuel mass through multiple injections promotes mixture homogenization and reduces the risk of wall impingement [15-16]. Moreover, multiple injections proved to be essential for the management of innovative combustion concepts, such as Low temperature Combustions (LTC) [17-19].

As widely described in the literature [20-23], in a GDI system operated with consecutive fuel jets, the first injection could strongly influence the behavior of the following, and the overall injected mass could significantly differ from the desired quantity. This result is due to the superposition of two effects: an electro-magnetic phenomenon in the injector coil (the magnetization of the coil due to the previous injection has not completely disappeared before the SOI of the following) and the propagation of pressure waves in the feed duct between rail and injector [24]. With regard to the electro-magnetic phenomenon, Viscione et al. [25] demonstrated that the residual energy content on the secondary coil of the injector is directly related to the shape of the current driving profile and Dwell Time (DT) between the injections. In particular, the higher the residual energy in the coil (e.g., when small DT are actuated) the higher the slope of the subsequent current profile. Such electrical interference results in a greater mass of fuel injected. With regard to the fuel pressure fluctuation (well known in high-pressure common rail injection systems [22]), it is triggered every time the injector is opened, and it occurs in the feed duct between the rail and the injector until its energy is dissipated. Thus, if the following injection occurs before the wave is completely dissipated, the injector will experience an instantaneous upstream pressure deviation from the target value (typically the rail pressure) and it will deliver a varying mass, depending on the difference between rail pressure and the average of actual pressure at the injector inlet during the second injection.

This paper presents an innovative injection management strategy aimed at improving standard GDI injection controllers by modelling and coupling both the electrical and hydraulic behavior of the injection system (by means of properly calibrated look-up tables to represent both phenomena), while performing coupled injections. In the present work, a GDI injection system capable of delivering fuel at pressures up to 750 bar has been studied. Extensive experimental activity aimed at investigating the effects of different injection strategies (injections duration, number, and spacing) and rail pressures on the behavior of the GDI system has been conducted using an open vessel flushing bench. Since previous work analyzes how the electro-magnetic phenomenon impacts the behavior of the injection system, this paper focuses on the analysis and modeling of the high-pressure wave in the injection system. Moreover, the detailed knowledge of the GDI injection system behavior has allowed to develop an innovative model-based GDI injection controller (MPW). In order to demonstrate the practical application of the presented approach, the developed injection controller has been implemented in a Rapid Control Prototyping (RCP) system. Finally, the MPW strategy has been experimentally validated and the improvements in terms of injection mass controllability have been demonstrated by comparing the injected mass running the injection system in standard configuration and with the innovative model-based injection controller.

1. EXPERIMENTAL SETUP

The experimental activity has been carried out on a specifically designed high-pressure open vessel flushing bench fueled with Research Octane Number (RON) 95 commercial gasoline. In this layout, the high-pressure system [22] has been connected to a set of GDI injectors [26] provided by Marelli Europe S.p.A. through standard feed ducts. The experimental activity has been carried out by injecting fuel into air at atmospheric conditions (pressure and temperature were not conditioned/controlled). The consumption has been measured through an AVL balance 733s. Figure 1 shows a schematic of the hydraulic bench layout, where the Low-Pressure (LP) and High-Pressure (HP) lines are represented in yellow and red respectively, while the water cooling is depicted in blue. Moreover, the main characteristics of the injection system are summarized in Table 1.

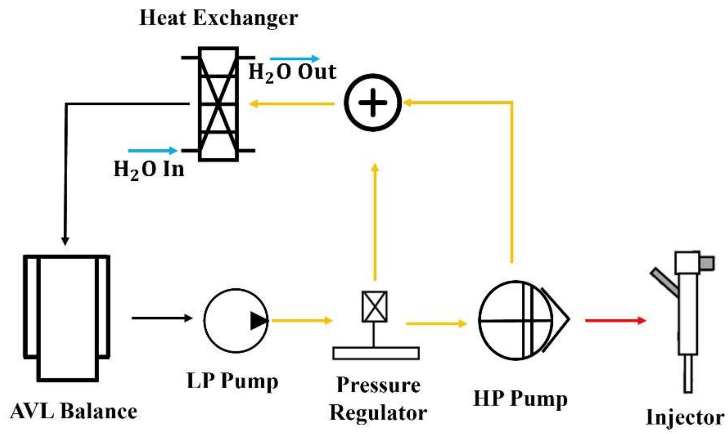

Figure 1: Flushing bench hydraulic layout

The LP line, between the LP pump and the HP pump, has been kept at a constant pressure of 4.5 barA through a mechanical pressure regulator. The return line of the pressure regulator has been connected with the return of the HP pump and water-cooled before mixing with the fuel coming from the AVL Balance. This configuration limits the increase in fuel temperature while the bench is operating. Moreover, to properly maintain at target value of the rail pressure, the HP pump has been equipped with a normally-opened solenoid metering valve Magnetic Proportional (MPROP). The return line of the MPROP has been directly sent to the AVL Balance.

Table 1: Injection System Characteristics

Number of Injectors	4
CR Pump	Bosch CP1
Injector Type	Marelli IVPH 700 bar [26]
Feed Duct Internal Length	29 mm
Feed Duct Internal Diameter	3 mm
CR External Length	19 mm

To monitor fuel pressure and temperature, additional transducers have been installed in the low-pressure line. With regard to the high-pressure line, where the only standard transducer available is the rail pressure sensor (PRail), to study pressure fluctuations and Residual Magnetization (RM) one of the high-pressure feed ducts (that delivers fuel from the rail to a specific injector) has been equipped with two piezoresistive high-pressure sensors Kistler 4067A: the first close to the rail (PKistRail) and the second close to the injector (PKistInj) (the distance between the two sensor is 19.9 cm) [25].

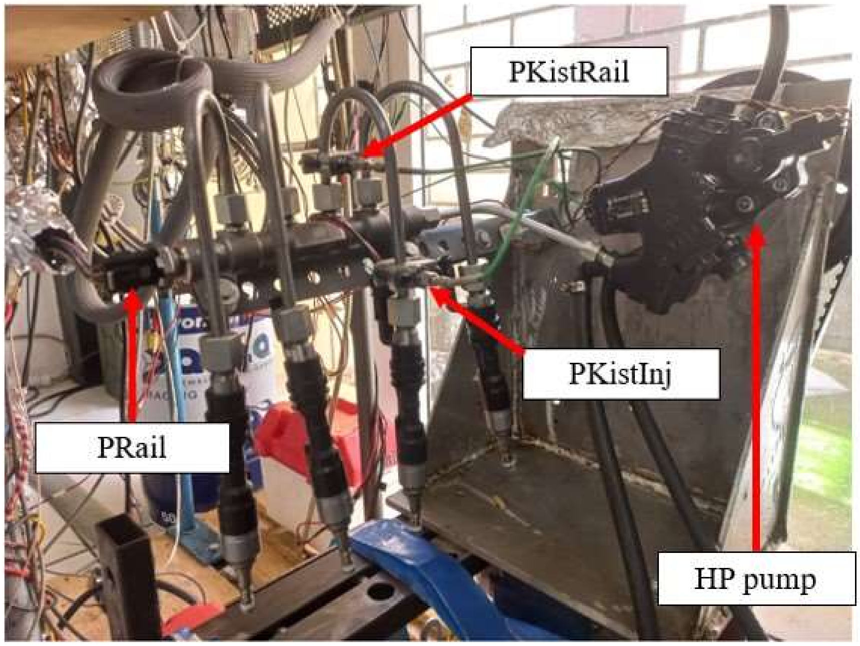

Figure 2: Position of pressure sensors and HP pump

To monitor the current driving profile, a current clamp Hioki CT6846A has been located in correspondence of the coil of the injector. The high-pressure sensors (PKistRail, PKistInj and PRail) and the current clamp have been acquired at 100 kHz to capture a higher-frequency content in the acquired signals, thus preventing aliasing in the sampling of pressure waves and injection commands. Moreover, to measure the HP pump speed, an optical encoder has been installed on the pump driveshaft. To properly control the flushing bench, and collect data coming from sensors, an RCP system based on a National Instruments cRIO 9082 has been developed. As shown in Figure 2, where the open vessel flushing bench is depicted, the high-pressure pump is mechanically connected through a toothed timing belt, with a fixed transmission ratio of 0.5 (replicating the on board GDI pump connection), to an electric motor (5.5 kW maximum power @3000 rpm). During the whole testing campaign, the speed of the HP pump has been kept constant at 500 rpm directly controlling the speed of the electric motor. This value has been selected since higher frequencies lead to an electro-magnetic interference between the modulation of the inverter and the signals detected by the RCP system. However, the presented approach remains valid also for different rotational speeds. As regards the rail pressure, it has been kept at a target value through proper management of the Pulse Width Modulation (PWM) command of the MPROP valve. To ensure a flexible control of the whole injection pattern, both in terms of rail pressure, number of injections, duration, and relative distance between the fuel jets, a fully programmable Electronic Control Unit (ECU), SPARK by Alma Automotive, has been adopted. Finally, to log the parameters of the injection controller and improve testing operations, INCA software (by ETAS) has been used. Figure 3 shows the complete layout of the control and acquisition systems.

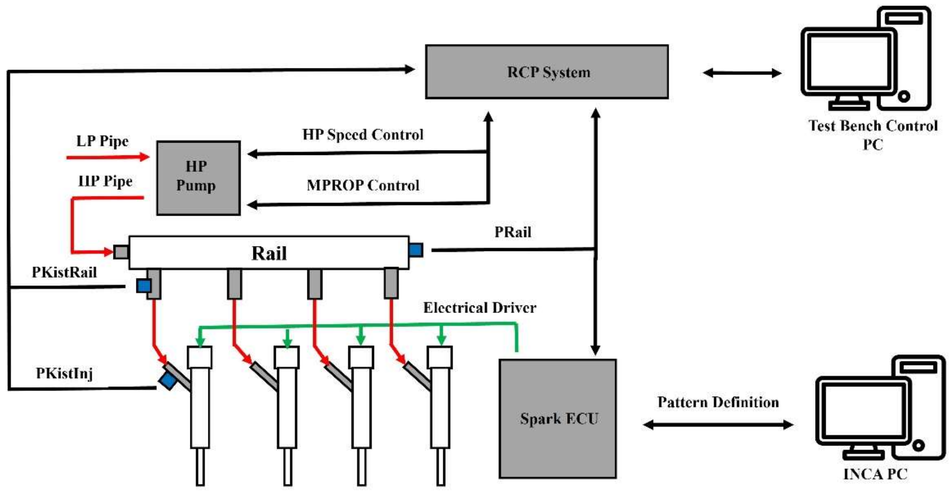

Figure 3: Control and acquisition systems layout

2. RESIDUAL MAGNETIZATION MODELING

In this section, the behavior of the injector under a double injection strategy in terms of total injected mass as a function of DT has been investigated. Figure 4 depicts the trend of the total injected mass performing two consecutive injections (same pulse duration on both injections equal to 700 µs) as a function of DT for three levels of rail pressure: 300 bar, 500 bar, and 700 bar.

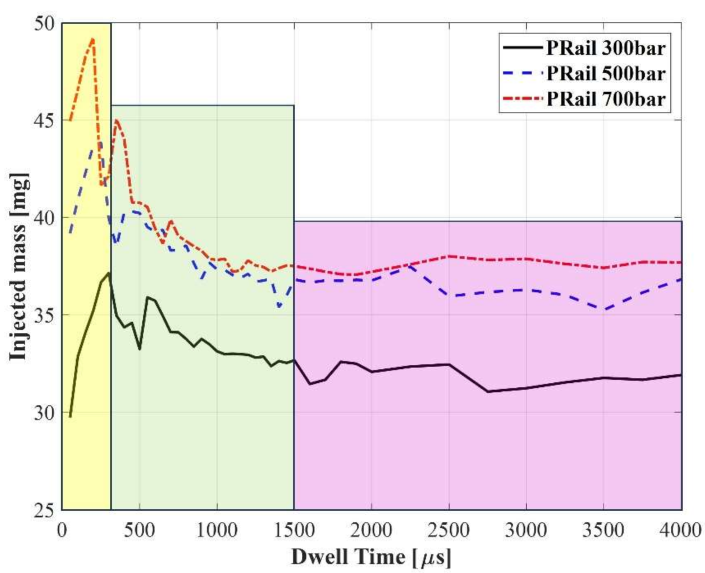

Figure 4: Total injected mass as a function of DT for first and second nominal injection duration of 700 µs for PRail of 300 bar (black line), 500 bar (blu line), 700 bar (red line) and hydraulic overlap (in yellow), transition region (in green) and stable region (in purple)

By looking at Figure 4, three different regions can be identified: DT from 0 to 350 μs called “hydraulic overlap”, where the injector operates in the hydraulic fusion region and the second injection starts before the injector needle comes back to the closing position; “transition region”, where DT ranges between 350 μs and 1500 μs, with a clear decrease of the measured injected mass; “stable region”, DT from 1500 μs up to 4000 μs, shows a stable value of the injected mass in the whole range of DTs.

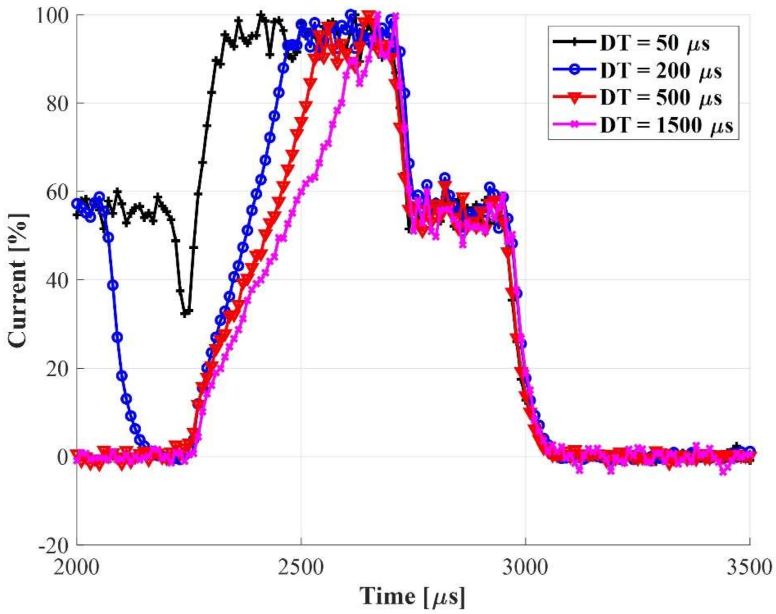

Figure 5: Current profiles for different DTs synchronized with the EOI of the second injection

To highlight the influence of electro-magnetic effects on the current driving profiles performing double injections, four different DTs (both injections have the same duration) have been compared and synchronized with respect to the descendent slope of the second injection (End of Injection, EOI), as shown in Figure 5. As it is possible to see, the lower the DT, the steeper the driving profile during the opening phase of the second injection. This aspect is mainly related to the amount of energy not yet dissipated in the injector coils and, as it is possible to notice, it leads to an increase in the effective opening time of the injector during the whole injection process [25]. Focusing the attention on the range of maximum interaction (DT = 50 μs to 500 μs), the response time of the electrical opening command of the injector (time to reach 100% of the driving profile) is significantly lower with respect to the one needed in unmagnetized condition (DT = 1500 μs), resulting in a higher injected mass. This behavior can be explained by referring to the residual energy content in the coils, which is high for close injection, then damps out as the dwell time exceeds 1500 μs. To characterize the amount of energy stored in the injector coils, the charge (Q) has been calculated by Equation 1, where i represents the acquired current of the injector driving profile:

$$Q = \int_{SOI}^{EOI} i(t)dt \qquad (1)$$

Differences between the charges of the driving unmagnetized and magnetized profiles have been calculated as a function of DT. The equivalent unmagnetized driving profile has been obtained by rigidly translating the electrical profile of the first injection pulse (which is unaffected by the magnetization) using the EOI of the second injection for synchronization. Figure 6 reports the signal manipulation process used to compare different driving profiles (unmagnetized and magnetized) at DT = 50 μs. As shown in Figure 6, the yellow area represents the nominal overlap between the two profiles. The green region, which lies between the equivalent unmagnetized profile (blue trace) and the magnetized profile (black trace), as well as the reference signal (red trace), stands for the RM effect. As DT increases the hydraulic fusion region ends and the magnetized profile reaches 0% current during the closure phase: in this situation the RM is calculated as the area between the magnetized profile and the equivalent unmagnetized one.

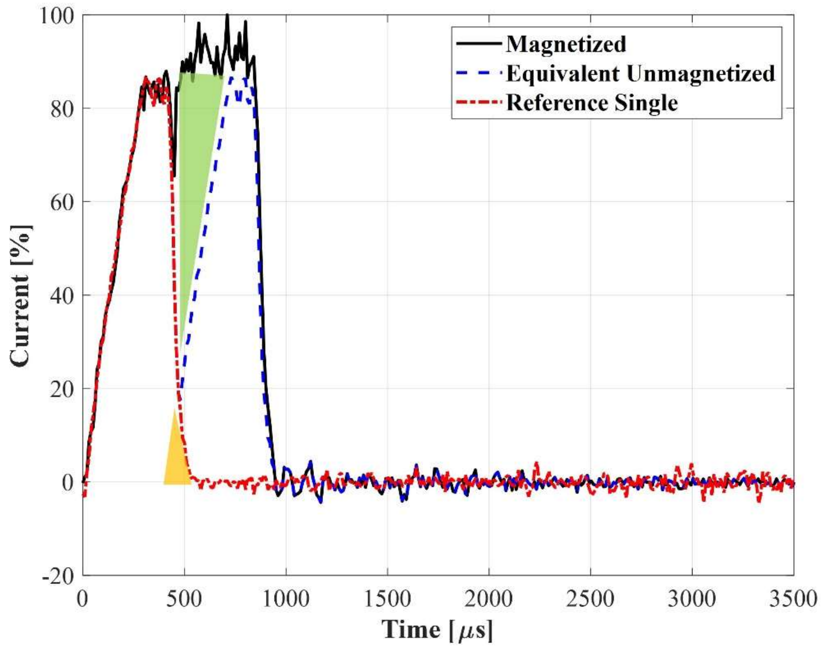

Figure 6: Example of magnetized (black), unmagnetized (blue), overlap area (yellow), RM area (green)

In Figure 7, the magnetized equivalent charge (A1: blue curve) is compared with the equivalent unmagnetized (A2: black dashed). As previously described, the overlap reduces the effective charge in the coil, and its effect is appreciable in the first part of the A2 curve. Finally, in order to keep into account both effects (overlap and magnetization), the difference between the two curves (A3: red dotted), has been calculated. As expected, the A3 curve shows a decreasing trend with the increase of the DT.

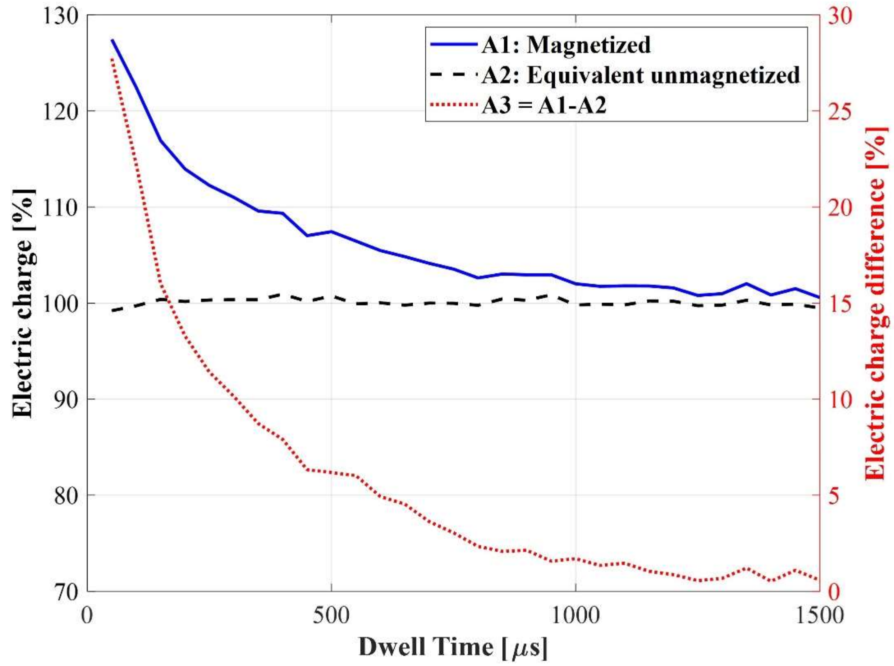

Figure 7: Equivalent charge for magnetized and unmagnetized profiles

Since the RM produces a higher injected mass, its effect can be described as an increment in ET with respect to the nominal injection duration. The Equivalent ET (ET_{eq}), defined in Equation 2, represents the ET for the second injection (in a two injection pattern with a standard duration equal to ET_1) that keeps into account the RM [24]. Figure 8 and Figure 9 report examples of ET_{eq} trend as a function of DT with different injection pressures and durations (both injections have the same ET). It is worth pointing out that the different profiles in Figure 9 collapse in a single curve if each profile is normalized with respect to the ET_{eq} at regime (when it reaches the nominal ET value).

$$ET_{eq} = \left[\frac{A_3(DT)}{\max\,(A_3(DT))} + 1\right] * ET_1 \tag{2}$$

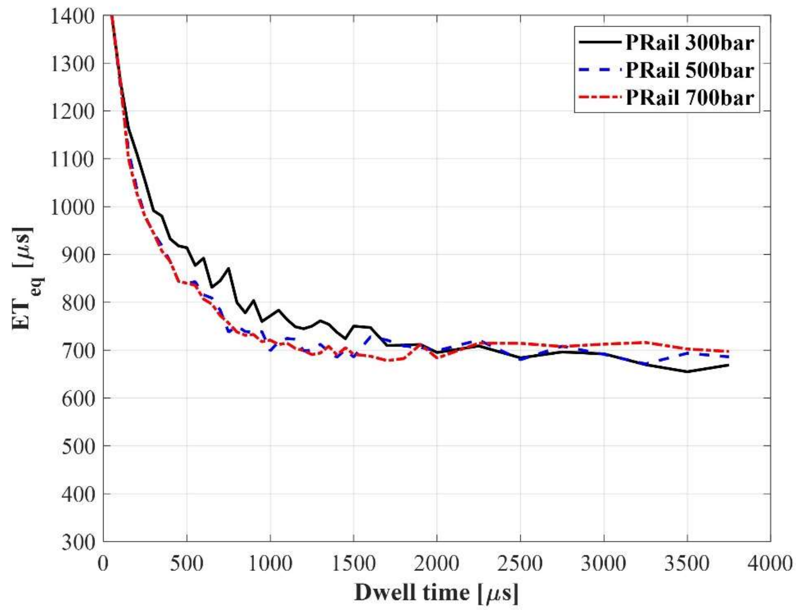

Figure 8: Equivalent ET as a function of DT for pulses nominal duration of 700 µs for PRail of 300 bar (black line), 500 bar (blue line) and 700 bar (red line)

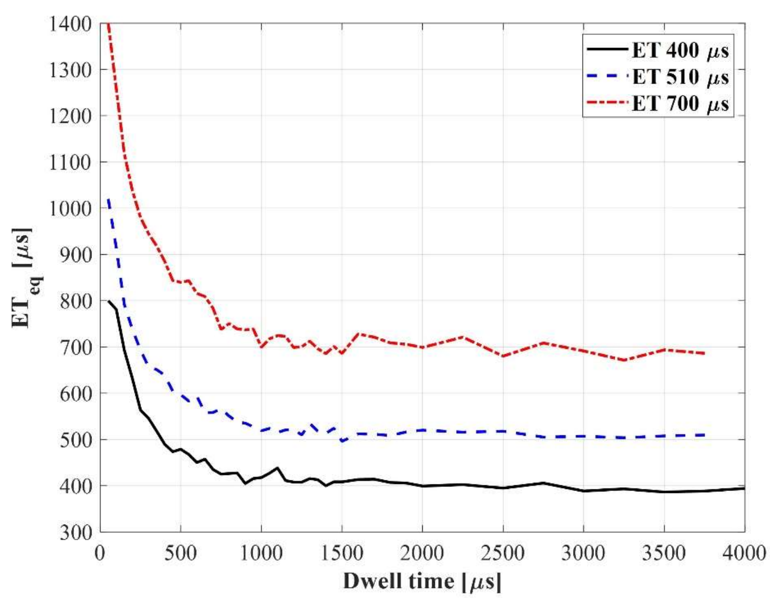

Figure 9: Equivalent ET as a function of DT for PRail equal to 500 bar and pulses nominal duration of 400 µs (black line), 510 µs (blue line) and 700 µs (red line)

As Equation 2 describes, ET_{eq} depends only on RM, overlap and first injection duration, while any dependence with respect to the pressure can be neglected [25]. In Figure 10, the map of ET_{eq} is presented as a function of the nominal pulse duration of the second injection (ET_2, since $ET_2 = ET_1$) and DT.

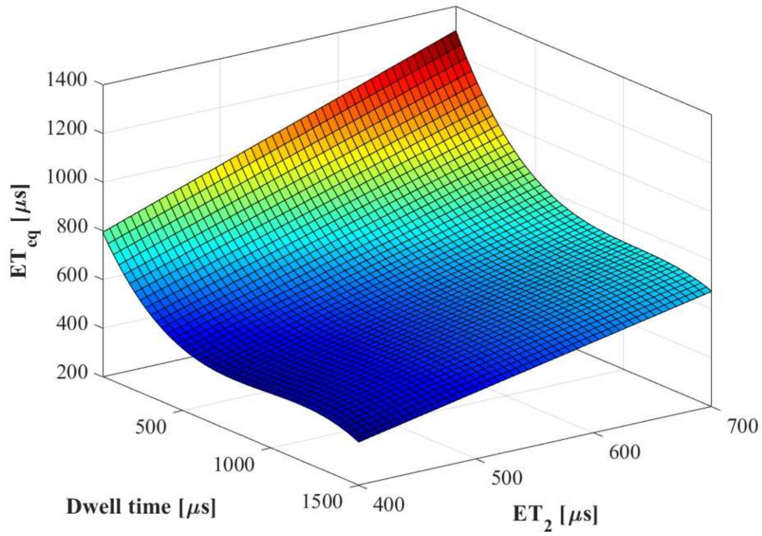

Figure 10: Equivalent ET map

In order to validate the presented method, the estimated injected mass for the second injection pulse in a double injection pattern has been calculated, with the procedure schematized in Figure 11. At first, the target mass of the second injection (m_2) has been converted into the injection durations (ET_2) through the injector map interpolation (actual PRail has been considered) neglecting the RM effect. Thus, by using the map shown in Figure 10, the RM effect has been taken into account with the ET_{eq} calculation (greater than ET_2) as a function of DT and ET_2 (with $ET_2 = ET_1$). At that point, the obtained equivalent ET and the acquired PRail have been used to interpolate the injector map estimating the mass injected during the second injection.

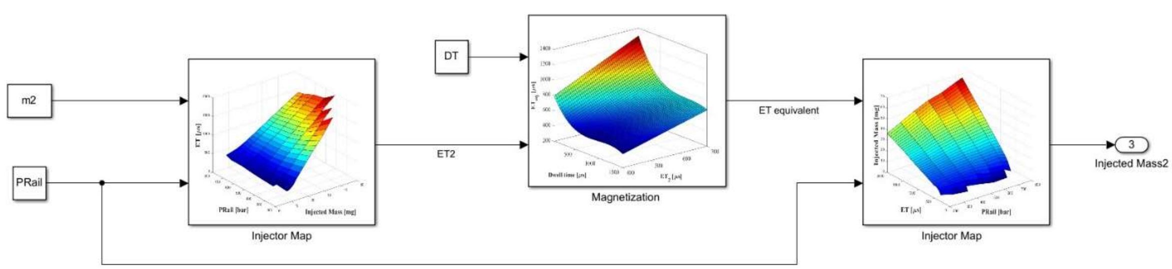

Figure 11: Procedure for the calculation of the injected mass under magnetized conditions

In Figure 12, the comparison between acquired (through the flushing bench, black solid curve with squares) total injected mass ($m_1 + m_2$, where m_1 represents the target injected mass in the first injection and m_2 in the second injection) and estimated (blue solid curve with dots) performing double injection strategy (where $m_1 = m_2$) has been reported.

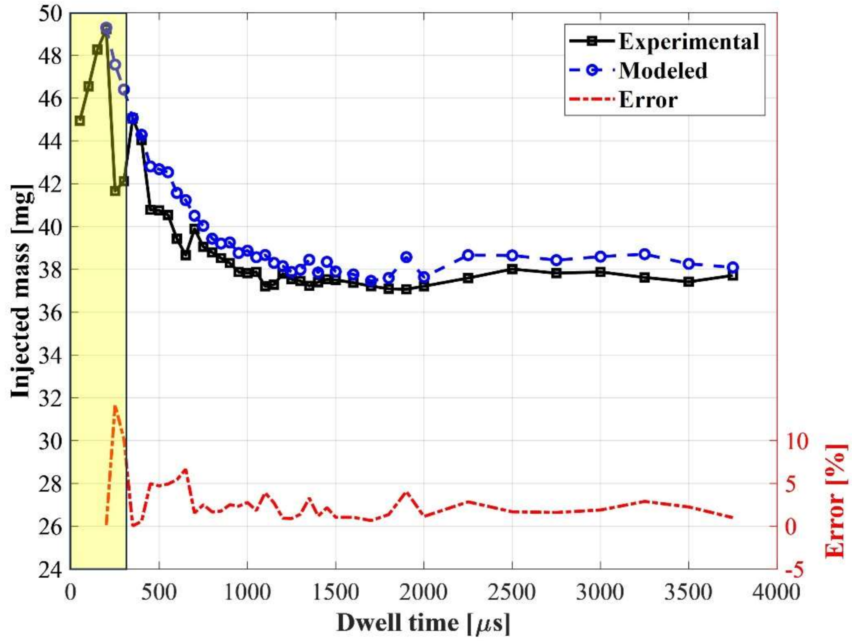

Figure 12: Comparison between experimental consumption under magnetized conditions (black curve), estimated one (blue curve), relative error (red curve) and hydraulic fusion region (in yellow)

As Figure 12 shows, the relative error (red dotted curve) is always below 6%, except for the hydraulic fusion region (yellow area, between 50 μs and 500 μs) where a peak value of 14% is reached. However, even at high DT (higher than 1500 μs), the model cannot accurately predict the behavior of the injector; in fact, the injected mass predicted by the model is about 2% higher than that measured one. As a matter of fact, since the model relies on the value of the rail pressure, which could be slightly higher than the actual the injector is subject to during the second injection (due to the pressure fluctuations in the feed duct of the injector), the modelled injected mass is usually overestimated. Therefore, to improve the estimation of the injected mass, it is critical to also develop a model that predicts the instantaneous pressure inside the injector feed port. Such a model will be discussed in the next section.

3. PRESSURE WAVES PHYSICAL MODEL

In this section, a detailed analysis of pressure dynamics that take place in the feed ducts of the injectors is reported. Several authors [25–28] already analyzed the pressure fluctuations that occur in high-pressure injection systems. However, most of these studies are focused on CR high-pressure injection systems for compression ignited engines. To model the hydraulic behavior of the system reported in Figure 2 [22], a wide experimental activity, summarized in Table 2, has been carried out performing both single and double injections (different DT with the same injection durations, $ET_1 = ET_2$). The tests have been run activating one single injector, while the remaining 3 injectors of the system have been kept inactive (but connected to the rail).

Table 2: Summary of experimental activity tests

<table>
<tr><th>Injection Type</th><th>Rail Pressure [bar]</th><th>ET1[μs]</th><th>ET2[μs]</th><th>DT [μs]</th></tr>
<tr><td>Single</td><td>200:100:700</td><td>350:100:1950</td><td>-</td><td>-</td></tr>
<tr><td>Single</td><td>750</td><td>350:100:1950</td><td>-</td><td>-</td></tr>
<tr><td>Double</td><td rowspan="3">300</td><td>400</td><td>400</td><td rowspan="9">50:50:1500</td></tr>
<tr><td>Double</td><td>450</td><td>450</td></tr>
<tr><td>Double</td><td>700</td><td>700</td></tr>
<tr><td>Double</td><td rowspan="3">500</td><td>400</td><td>400</td></tr>
<tr><td>Double</td><td>510</td><td>510</td></tr>
<tr><td>Double</td><td>700</td><td>700</td></tr>
<tr><td>Double</td><td rowspan="3">700</td><td>400</td><td>400</td></tr>
<tr><td>Double</td><td>600</td><td>600</td></tr>
<tr><td>Double</td><td>700</td><td>700</td></tr>
</table>

Figure 13 reports an example of acquired pressure signals: PRail (grey), PKistInj (red) and PKistRail (blue).

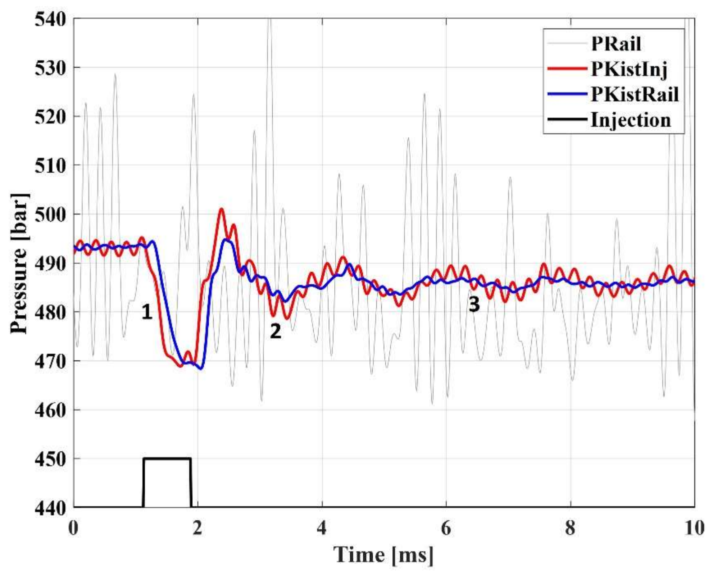

Figure 13: Experimental pressure traces of the three signals for a single injection at 500 bar, ET 750 µs: PRail (grey line), PKistInj (red line), PKistRail (blue line), injection command (black line)

Analyzing the acquired signals immediately after the SOI, it is possible to notice a sudden drop of the pressure in both PKistRail and PKistInj traces, while such information is not clearly visible in the PRail signal. This aspect can be easily explained by the amount of fuel mass contained in the rail (compared to the feed duct) which limits the effects of the wave propagation. Even if PKistRail and PKistInj signals show the same behavior in terms of oscillations, the drop phase in PKistRail is slightly retarded with respect to PKistInj. In fact, the high-pressure wave (generated by the injector opening), moves backward to the rail. As a consequence, the PKistRail sensor experiences a pressure drop slightly later. Focusing the attention on the PKistInj signal, three different phases can be identified [31]: the first stage (point 1 in Figure 13) refers to the abrupt pressure drop caused by the injection, the second (point 2) features the high-pressure oscillation where the wave triggered by the injection propagates back in the feed duct, while the last (point 3) is the pressure recovery stage, where the high-pressure wave is almost completely dissipated. Due to the position of PKistInj with respect to the injector, this sensor perceives the injector's upstream pressure: for this reason, the modelling of the hydraulic behavior has been based on the information contained in the corresponding signal. In addition, to increase the robustness of the modelling approach by analyzing only the pressure wave caused by the injection event (i.e., removing noise), the average of the pressure signal acquired over 500 consecutive cycles has been considered. The average pressure trace presents a well-defined shape, typical of the underdamped mass-spring-damper system, as shown in Figure 14.

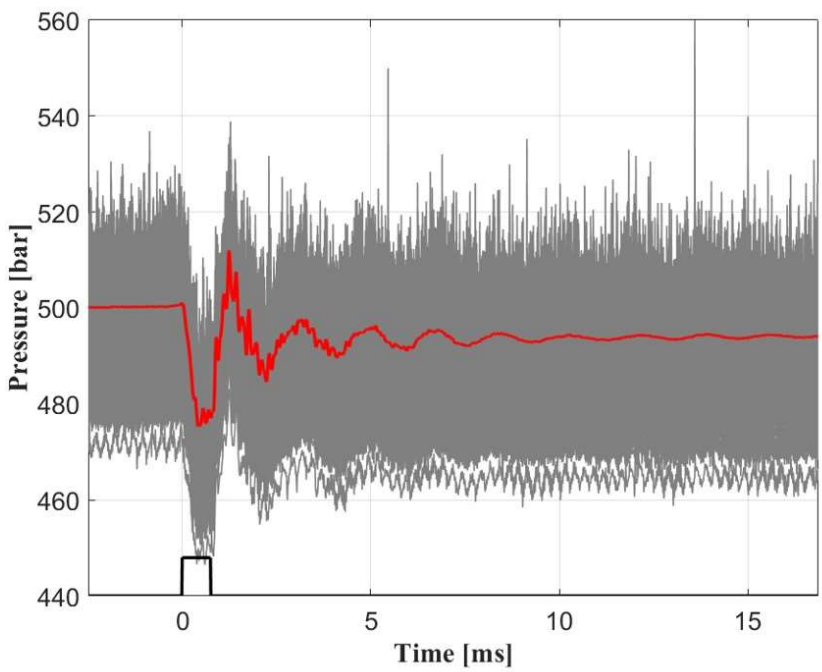

Figure 14: PKistInj signals of 500 consecutive cycles (grey lines) and the mean one (red line) for 500 bar, ET 750 µs

The behavior of the hydraulic system can be described as a free response of a one-degree-of-freedom Mass Spring Damper (MSD) [22] system described in Equation 3, where *x* represents the pressure, *m* represents the fuel inertia, *c* is the equivalent damping and *k* the equivalent stiffness.

$$m\ddot{x} + c\dot{x} + kx = 0 \tag{3}$$

It is possible to define the natural frequency ω_n of the system and the damping ratio ξ, as in Equations 4 and Equation 5 respectively.

$$\omega_n = \sqrt{\frac{k}{m}} \tag{4}$$

$$\xi = \frac{c}{2\sqrt{km}} \tag{5}$$

Moreover, it is important to define the oscillating frequency ω_d in under-damped conditions as reported in Equation 6:

$$\omega_d = \omega_n\sqrt{1-\xi^2} \tag{6}$$

The free response of the system is described by Equation 7 where x_0 and v_0 represent the initial conditions at t = 0.

$$x(t) = e^{-\xi\omega_n}\left[x_0\cos(\omega_d t) + \frac{v_0 + \xi\omega_n x_0}{\omega_d}\sin(\omega_d t)\right] \tag{7}$$

To understand how many free responses are needed to describe the hydraulic system under study (the overall system behavior will be the result of the superposition of several MSD free responses [22]), the power spectrum of experimental pressure waves under different conditions has been studied. Figure 15 shows an example of the power spectrum for three different values of rail pressure obtained running single injection at a constant ET of 700 µs.

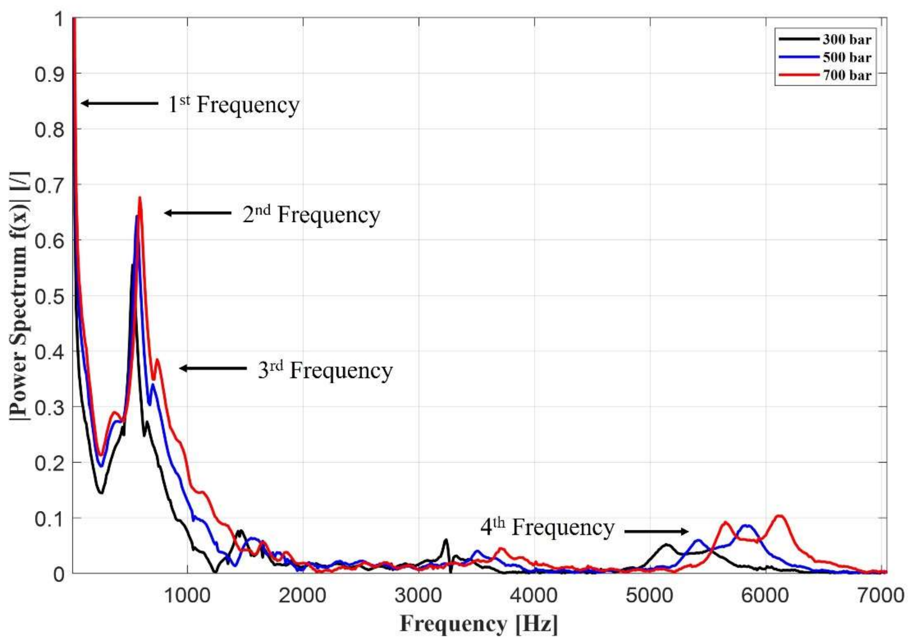

Figure 15: Power spectrum for ET equal to 700 µs for three different values of the rail pressure: 300 bar (black line), 500 bar (blue line) and 700 bar (red line)

From the analysis of the power spectrum reported in Figure 15, four characteristic frequencies can be clearly identified: the first frequency at 8.33 Hz is related to the injection frequency; the second, between 520 Hz and 590 Hz; the third, between 650 Hz and 740 Hz, and the fourth, between 5 kHz and 6.5 kHz. The first frequency can be neglected because it does not represent the dynamic system response but only the external trigger (injection event). The second frequency can be considered as the main carrier of the system, because it shows the highest amplitude in all the operating conditions. On the opposite, since it does not exhibit a high amplitude and its relative frequency distance from the main carrier is limited (as previously demonstrated by Silvagni et al. [22]), the third carrier can be disregarded. Finally, despite its low amplitude, the fourth main frequency cannot be neglected, mainly because such contribution is clearly visible in a relatively high-frequency range. Therefore, in order to properly model the pressure fluctuations both second and fourth harmonics are required. Moreover, since the frequencies of the pressure waves are proportional to the speed of sound (which is affected by the bulk modulus of the fluid), the power spectrum shifts to higher frequencies with the increase of the rail pressure [31].

In order to reconstruct the single-injection pressure wave propagation as the sum of free responses of the system, the characteristic parameters (ω_n, ξ, x_0, v_0) of each characteristic carrier (second and fourth frequencies) have been calculated through a numerical procedure using MATLAB code. The numerical algorithm minimizes the distance between the modulus between the actual pressure trace, filtered across the considered carrier (one at a time), and the 1 Degree of Freedom (DoF) MSD parametric free response reported in Equation 7. This procedure has been applied for each pressure trace for the two identified characteristic carriers.

Figure 16 and Figure 17 show the maps of the 1-DoF MSD system characteristic parameters for each carrier as a function of injection pressure and ET.

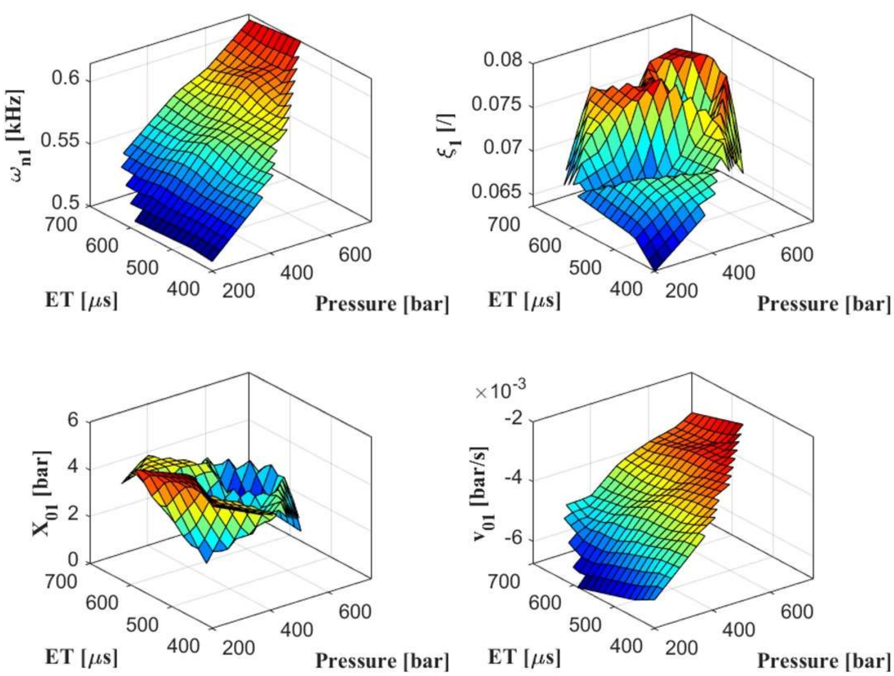

Figure 16: Characteristic parameters for the first carrier as a function of PRail and ET: ω_{n1} (a), ξ_1 (b), x_{01} (c), v_{01} (d)

By looking at the maps of the first carrier, it can be noticed that both ω_{n1} and v_{01}, Figure 16 a) and d) respectively, are linearly dependent on the injection pressure while the dependence on the injection duration is significantly lower. Figure 16 c) shows the trend of x_{01} as a function of ET and rail pressure. The map of ξ_1

(Figure 16 b) does not report a clear tendency. However, due to the very limited range of variation of ξ_1, its value can be considered constant for the following modeling process.

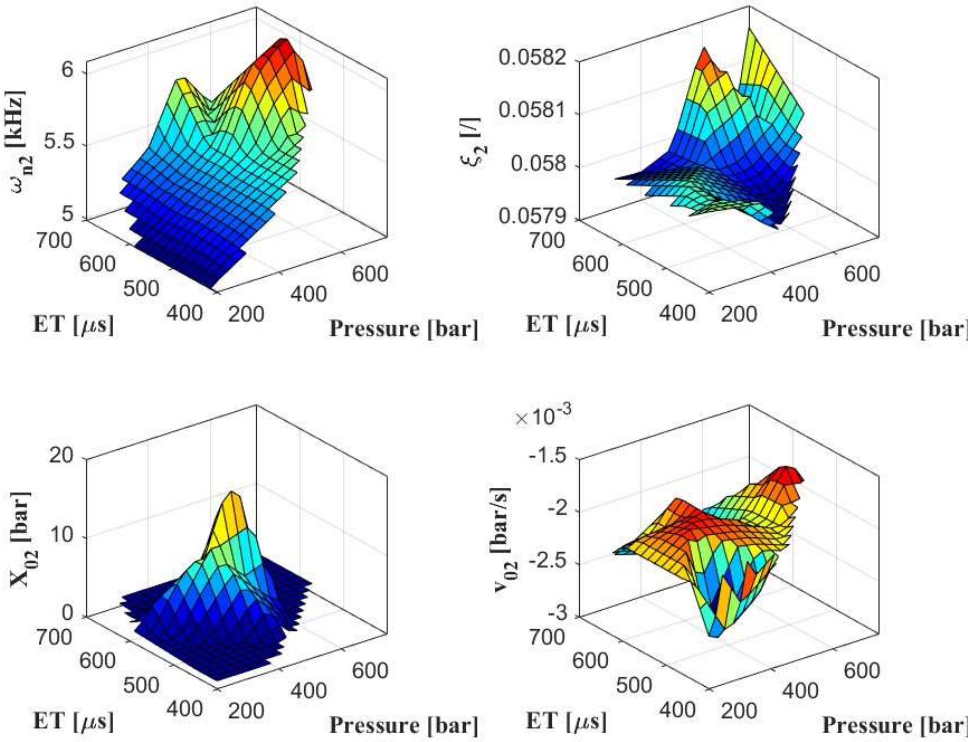

Figure 17: Characteristic parameters for the second carrier as a function of PRail and ET: ω_{n2} (a), ξ_2 (b), x_{02} (c), v_{02} (d)

Analyzing the maps of the second carrier also ω_{n2}, as expected, shows a linear trend with the rail pressure, ξ_2 which can be considered constant for all the conditions as well as v_{02}. Finally, x_{02} becomes different from zero at intermediate values of rail pressure and pulse duration.

4. RESULTS AND DISCUSSION

In the following sections, an innovative injection management strategy aimed at improving standard GDI injection controllers, based on the combined modeling of both electrical and hydraulic behavior of the injection system, is described.

4.1 Pressure Wave Reconstruction

In order to accurately calculate the ET_{eq} described in section 3, the pressure fluctuation in the feed duct of the injection system under study has to be reconstructed.

4.1.1 Pressure Wave Reconstruction for Single Injection

As reported in previous works [22], the injection system hydraulic behavior performing multiple injections can be described as the superposition of two reconstructed injection pressure traces triggered by a single injection event. In the case of single injection event, an estimation of the pressure fluctuation can be obtained using the scheme shown in Figure 18: the rail pressure and ET of the injection triggering the pressure wave are used to interpolate the maps of the characteristic parameters for the 1-DoF MSD equivalent systems of the 2 selected carriers. Moreover, Gain and Offset maps are interpolated in the same way to obtain a complete reconstruction of the pressure trace. The Offset map represents the mean value of the pressure wave (lost during the reconstruction, since the fundamental component is not modelled) [22] which is lower than the PRail since the pressure in the duct is not recovered even after several milliseconds, as appreciable in Figure 13. As regards the Gain map, it is necessary to compensate for the loss of information due to the fact that only two harmonics of the spectrum are considered [22].

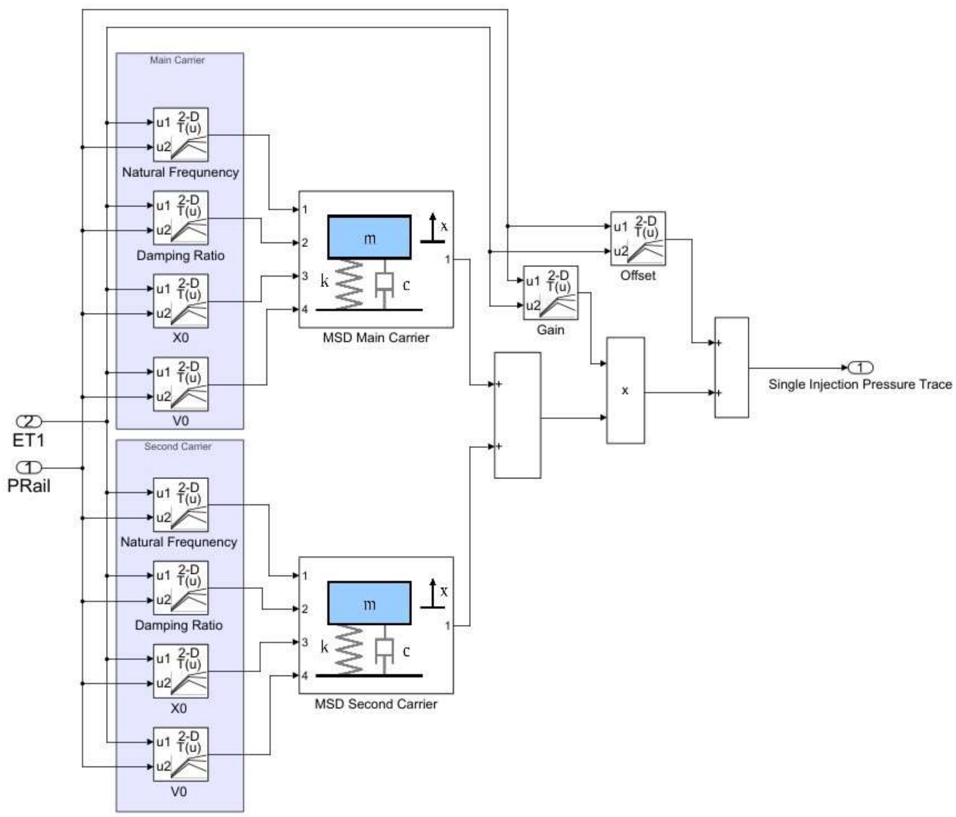

Figure 18: Single injection reconstruction strategy

In order to evaluate the accuracy of the proposed methodology, the percentage error between acquired and modelled pressure traces has been calculated. Figure 19 compares the predicted and the experimental pressure trace from the PKistInj in different conditions of rail pressure and ET. As it can be seen, the error, defined as the difference between the acquired and the estimated pressure oscillation, is always between +/-5 bar with the exception of the zone immediately after the injector closing (such area is out of the nominal operating range of GDI injection systems).

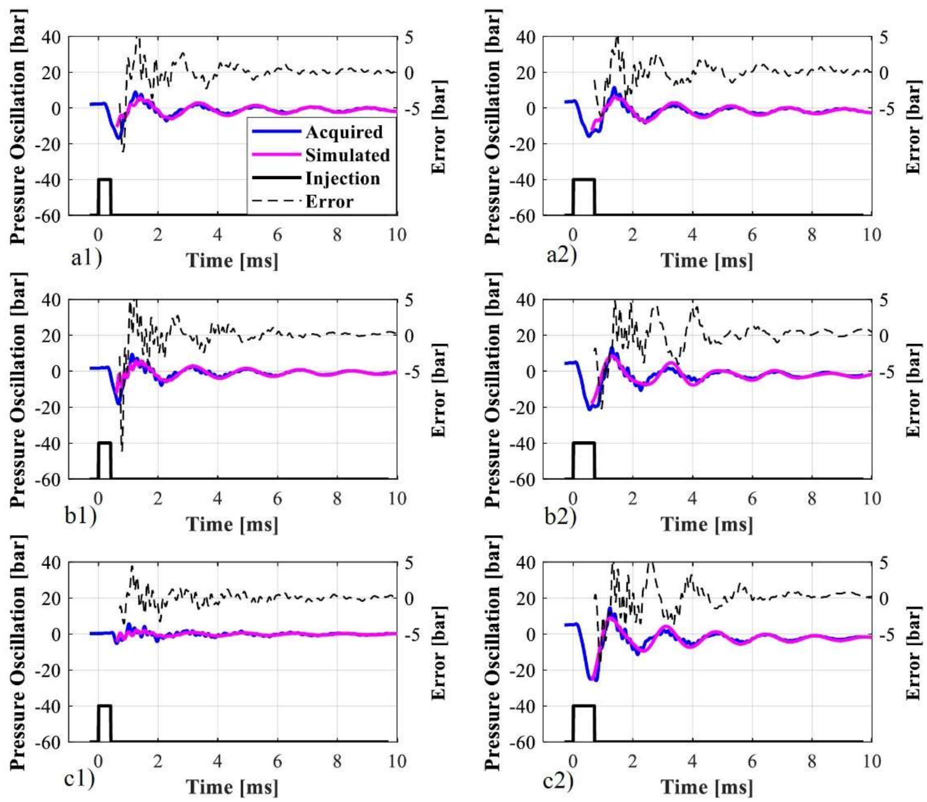

Figure 19: Experimental pressure traces (blue curves) and modeled (purple curves) for 300 bar (a), 500 bar (b) and 700 bar (c), for ET of 400 µs (numbers 1) and 700 µs (numbers 2)

4.1.2 Pressure Wave Reconstruction for Double Injection

As mentioned in the previous section and described by several authors [17–19, 30, 31], the proper management of the injection pattern is crucial to guarantee proper combustion stability and controllability [34]. However, the amount of fuel injected through the injection process after the first injection event is strongly affected by the pressure wave triggered by the first injection pulse (if the pressure wave is not yet completely damped). It is important to underline that, even if extremely high DTs are applied (i.e., 5 ms where the magnetization phenomena can be neglected), the pressure in the feed duct in the considered GDI injection system is still not recovered, resulting in a lower injected mass, compared to doubling a single injection event (if the same ET is applied).

In order to obtain the pressure traces generated in the feed duct when a double injection pattern is actuated, the acquired PKistInj signal during a double injection test has been deeply analyzed. Figure 20 shows the comparison between the measured pressure traces when a double injection (with $ET_1 = ET_2$, red trace) and a single injection are actuated (blue trace). Moreover, Figure 20 also reports the reconstruction of the pressure wave (magenta trace) for the double injection strategy, obtained superimposing to the rail pressure signal PRail two single injection pressure oscillation traces: the first wave starts from SOI_1, while the following occurs in correspondence of the considered DT (equal to1000 µs). The analysis of the relative error between the experimental (PKistInj) and reconstructed (PRail + pressure oscillations model) pressure traces confirms the accuracy of the presented modelling approach even in the case of multiple injection strategies.

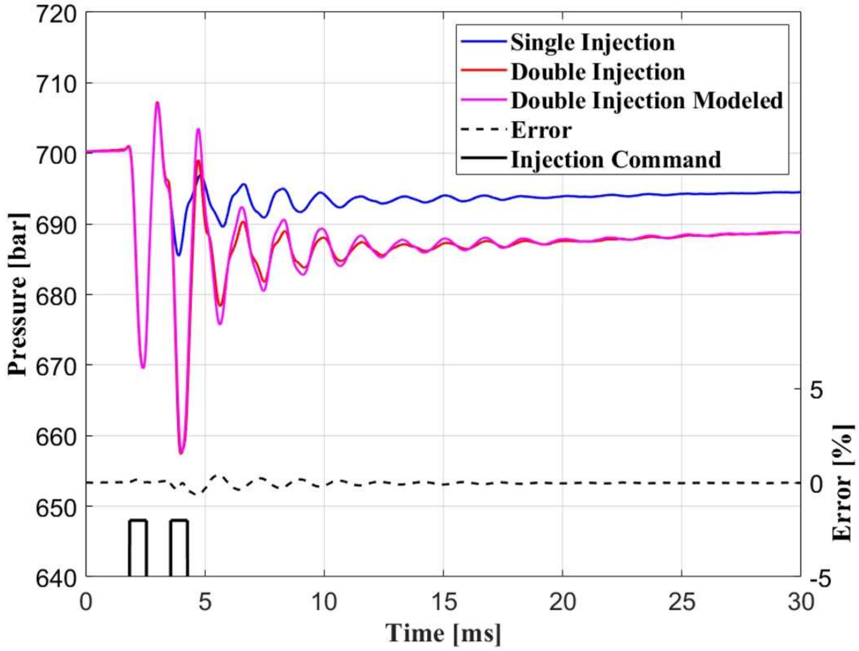

Figure 20: Comparison of single injection at 700 bar (blue curve) with an ET equal to 700 µs, a double injection at 700 bar with $ET_1 = ET_2 = 700$ µs and DT = 1000 µs (red curve), and the reconstructed pressure trace of the double injection obtained superimposing to the single injection wave itself, at the DT (purple curve)

A scheme of the methodology for the reconstruction of the pressure waves when a double injection pattern is used, is reported in Figure 21.

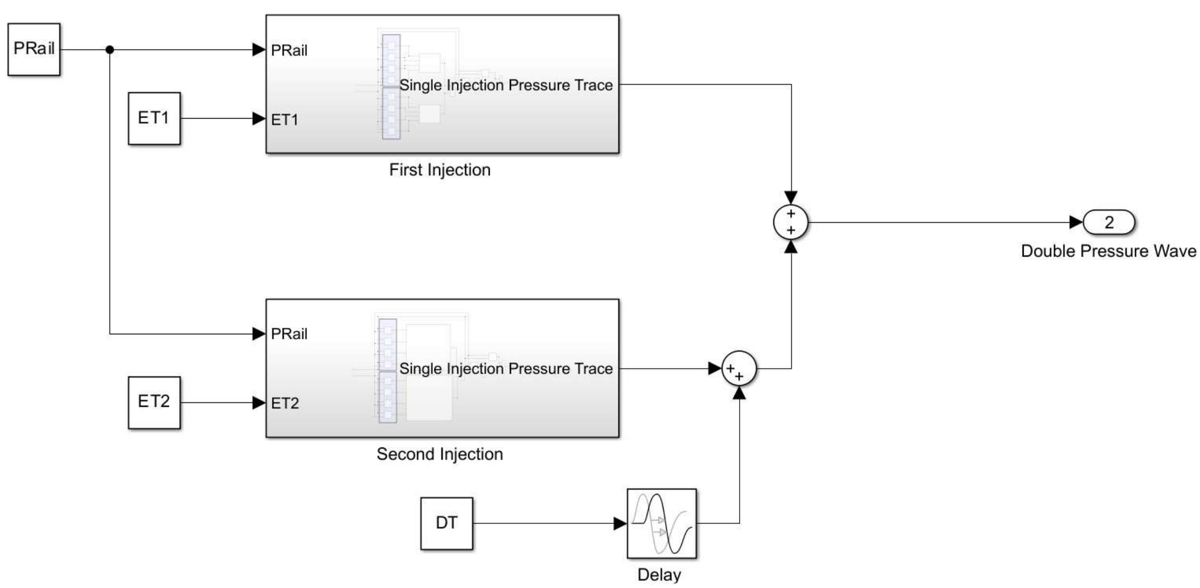

Figure 21: Double injection reconstruction strategy

Figure 22 shows the comparison between reconstructed and experimental pressure oscillations for double injection strategy at four different DTs of 300 µs, 500 µs , 750 µs, 1000 µs respectively (PRail approximately equal to 700 bar, $ET_1 = ET_2 = 700$ µs). For each condition, the analysis of the absolute error reported in Figure 22 demonstrates the capability of the reconstruction strategy to predict the pressure waves in the feed duct during a double injection pattern. As it is possible to see, during the second injection the error is always between +/-5 bar. As a result, the model can reliably estimate pressure fluctuations and the actual injection pressure even running double injection patterns.

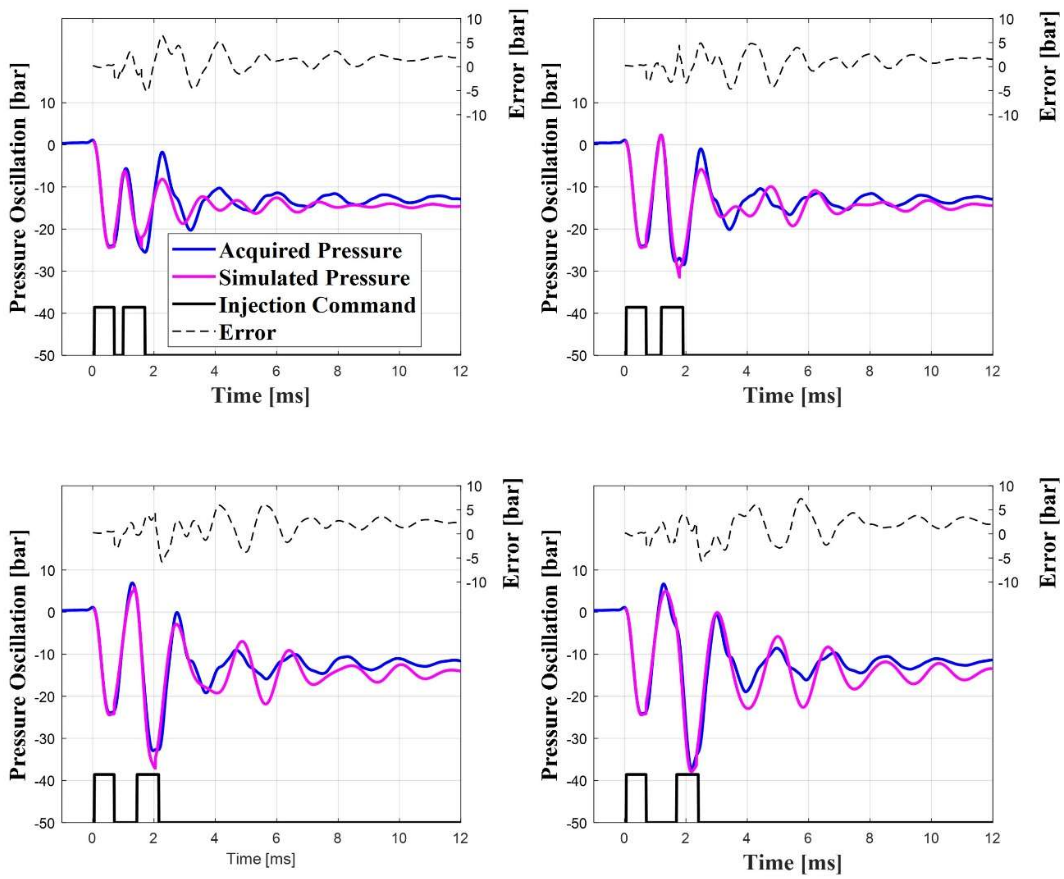

Figure 22: Comparison of experimental (blue curve) and simulated (purple curve) pressure traces for double injection strategy at PRail of 700 bar with ET1 and ET2 equal to 700 µs for DT equal to 300 µs (a), 500 µs (b), 750 µs (c) and 1000 µs (d)

Since the injected mass of the second fuel jet depends on the actual pressure acting on the injector during the second injection event (which can significantly differ from the pressure value in the rail, if a pressure wave is still present) and ET_2, the average of the acquired and the estimated pressure oscillation during the second pulse (in the analyzed condition, PRail = 700 bar and $ET_1 = ET_2 = 700$ µs) has been calculated (Figure 23). As it is possible to notice, the average pressure during the second injection is always lower than the rail pressure (which corresponds to a pressure value of 0 bar). This aspect explains the behavior of Figure 12, where the modeled mass shows an offset with respect to the experimental one (since the RM model relies on PRail). Therefore, the effect of the pressure oscillation is always to decrease the injected mass, with respect to the sum of two single injections performed under the same conditions of ET and rail pressure. The absolute error between the two pressure traces is always between +/- 3 bar, confirming the reliability of the presented method. However, the error between the two pressures slightly increases at higher DTs owing to an overestimation of the second pressure drop. This aspect is related to the procedure applied for the reconstruction of the wave. An offset is applied before the sum of the second wave to the first one, and it can be modelled as a constant value or as a function of DT. For the purpose of the present work, to perform accurate estimation below DT = 800 µs where the absolute value of the error is below 2%, such quantity has been considered as a constant being the objective

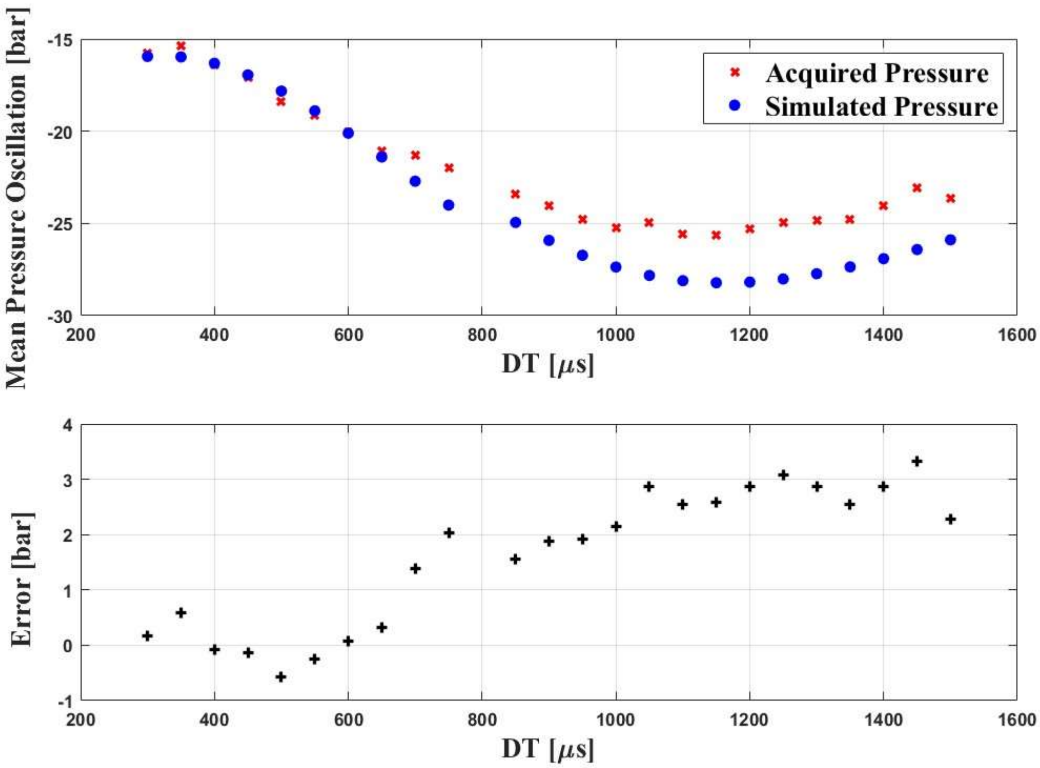

Figure 23: Mean pressure oscillation during the second injection for experimental (red crosses) and simulated (blue dots) pressure traces for PRail of 700 bar and pulses duration of 700 µs (a) and absolute error (b)

4.2 Equivalent Energizing Time Modeling for Pressure Wave

In the previous sections, the effect of the hydraulic interaction between two consecutive injections on the total amount of injected fuel has been deeply discussed. As a result, to optimize the combustion process when multiple injection pattern is used, a strategy which compensates for the injected mass deviations is mandatory.

In Figure 24, a schematic of a possible injection quantity controller for a double injection pattern (two small pilots are actuated with $\mathrm{ET_1} = \mathrm{ET_2}$) which compensates the pressure wave effect is presented. The first injection duration, $\mathrm{ET_1}$, is directly calculated from the injector map using the PRail signal and the requested mass $\mathrm{m_1}$ as inputs. On the contrary, since the injector map has been characterized in standard condition (a single injection pulse was actuated), $\mathrm{ET_2}$ can not be obtained in the same way because of the hydraulic dynamic interference between the injections. As a matter of fact, while for the first injection the PRail signal and the pressure at the injector inlet are nearly identical, when the second injection occurs the pressure facing the injector differs from the PRail due to the pressure wave propagating in the feed duct. Therefore, to properly compensate for such an effect, the second injection duration (ET_2) needs to be calculated using as inputs the target fuel mass for the second injection, m_2, and the actual average pressure for the second pulse. It is easy to understand that the cost of the sensors aimed at capturing the fuel pressure near the injector (similar to the PKistInj sensor) is not compatible with on-board mounting. As a result, an alternative approach, aimed at estimating the actual pressure during the injection process is mandatory. As previously described, the pressure wave can be accurately reconstructed starting from the 1-DoF MSD characteristics parameters mapping. Therefore, the presented methodology relies only on the 3D maps previously generated which can be implemented in a standard ECU without the need for any additional sensor.

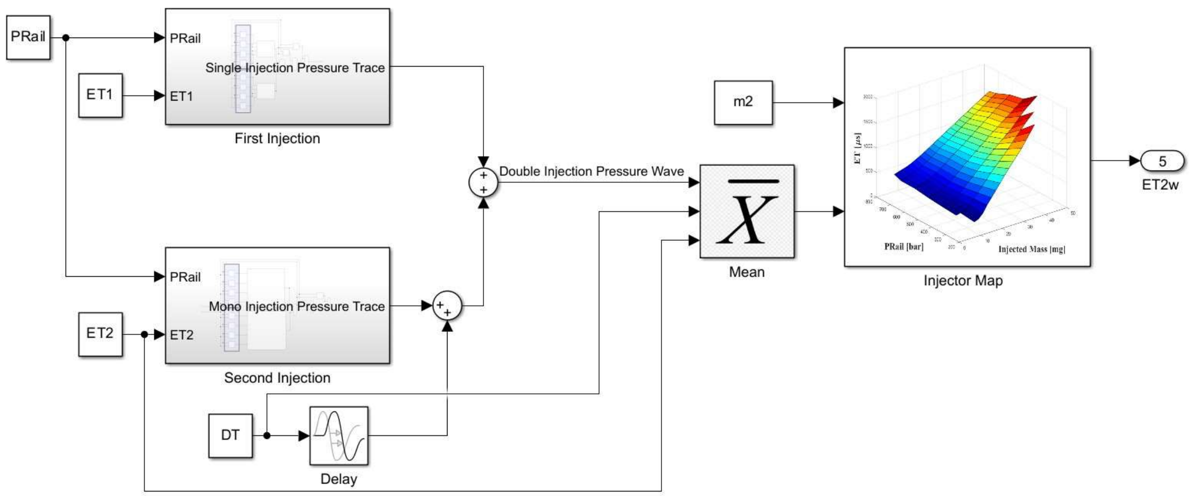

Figure 24: ET2w strategy for pressure wave compensation on the injected mass on the second injection

4.3 Equivalent Energizing Time Modeling for Residual Magnetization

Once the strategy for compensating pressure wave effects has been defined, to ensure proper control of the total fuel mass injected with the GDI injector, the effect of residual magnetization (RM) has to be accurately compensated. As explained in the literature [25], the electro-magnetic interactions can be compensated using a strategy based on the inversion of the previously discussed RM model, Figure 25. For each DT, the duration of the second injection needed to compensate for the residual magnetization ($ET_{2\_corrected}$) has been calculated through the map reported in Figure 25, with the current DT and ET_2.

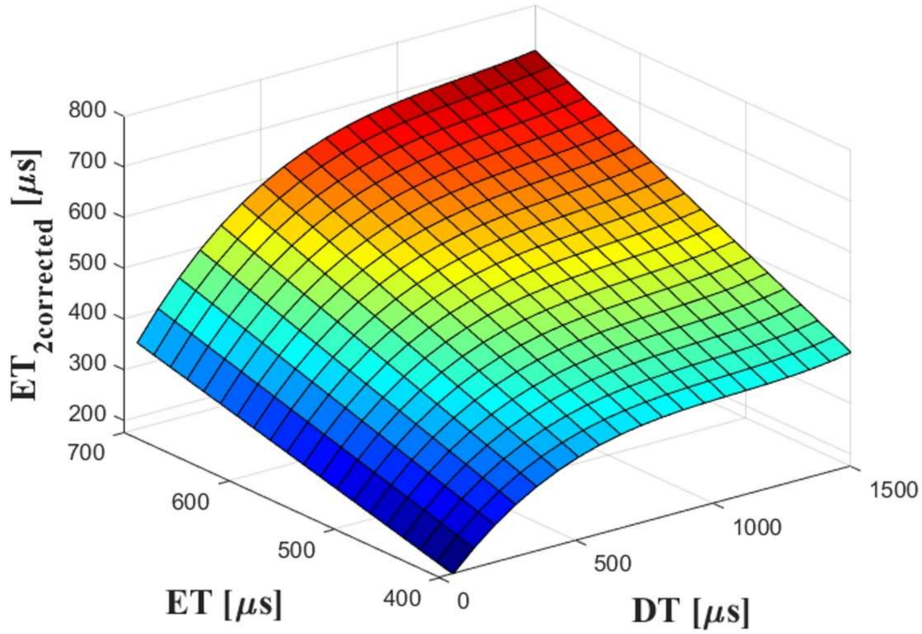

Figure 25: Map of ET corrected

Figure 26 shows an example of RM correction for a PRail of 500 bar and $ET_1 = ET_2$ equal to 700 µs. The DT sweep shown in Figure 26 has been performed by applying $ET_{2\_corrected}$ as the duration for the second injection pulse. It is possible to see that the RM correction methodology is capable of mitigating the incoherences in terms of total injected mass with respect to the uncorrected condition. However, although the RM compensation strategy is able to bring the value of the injected mass very close to the target value (defined as twice the mass introduced with the first injection), the injected mass remains below the reference even for DT values of 1500 µs ("stable region"). As previously discussed in paragraph 4.3, this phenomenon is generated by the pressure variation within the injector supply line (with respect to the PRail value). Therefore, even at high DT values, the overall injected mass remains below the reference mass. The following sections describe how the presented approach can be further improved through proper modelling of the pressure fluctuation in the injector feed duct.

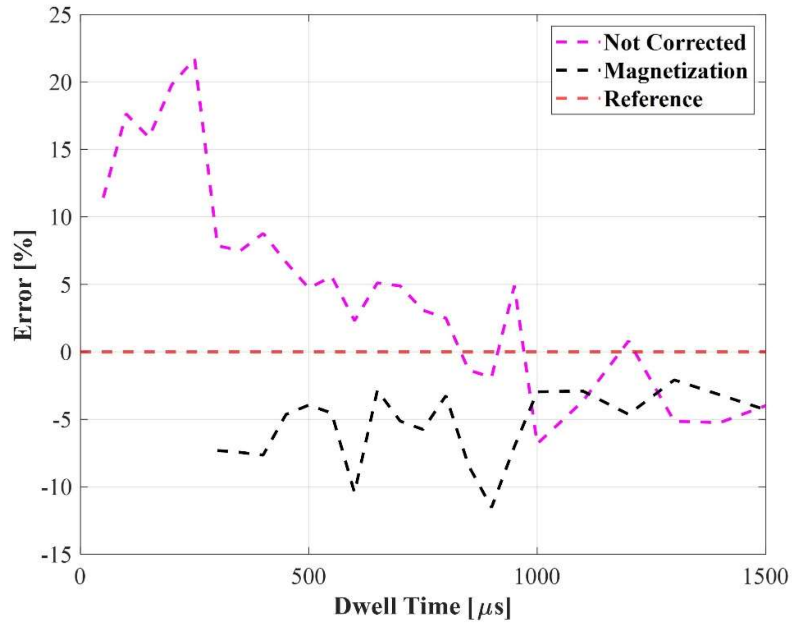

Figure 26: Comparison between not corrected and corrected fuel injected mass with 500 bar injection pressure and ET of 700 µs

4.4 MPW Correction Strategy

Cavicchi et al. [24] discussed the coupled effect of RM and pressure wave of a high-pressure GDI injector on the total injected fuel in a multiple injection pattern. As mentioned before, such aspects might become critical when running innovative high-efficiency combustion methodologies, characterized by a very small operating range. Therefore, a novel injection management strategy aimed at compensating at the same time RM and pressure waves effect (MPW correction strategy, Figure 27) has been developed and implemented in the RCP system.

The first step is the definition of the injection pattern parameters: rail pressure, target injection mass for both injection pulses and DT. From the target masses and PRail, ET_1 and ET_2 are calculated. The MPW correction strategy workflow starts compensating the RM effect: the corrected ET for the second injection ($ET_{2\_corrected}$) can be estimated starting from the ET_2 and the DT through the magnetization characteristic of the injector (determined as described in section 4.3, when $ET_1 = ET_2$). Therefore, the injector duration during the second pulse is now lower than ET_2, but the target mass of the second injection is guaranteed. Once the RM effect has been compensated, from PRail, ET_1, $ET_{2\_corrected}$ and DT, it is possible to estimate the pressure wave that would take place in the double injection pattern. Lastly, the final injection duration to be applied (ET_{2_Final}) can be defined and sent to the injection electrical driver.

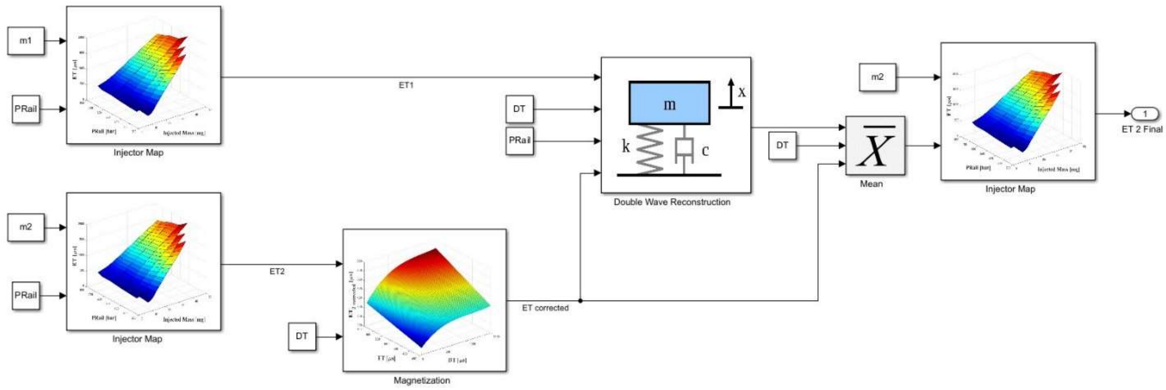

Figure 27: MPW correction strategy to compensate for both effect of RM and pressure wave

Figures 28 and 29 show a comparison of different compensation methodologies with the reference injected mass, using a pattern of two consecutive injections: no correction (purple dashed lines), only RM compensation (black dashed lines), and both RM and pressure waves compensations (blue dashed lines). As it is possible to see, the main correction contribution is related to the RM effect, while a secondary but not negligible correction, related to the pressure wave propagation, brings back the fuel consumption across the target value reported in the red dashed line for all the tested conditions (PRail = 500 bar and m_{tot}39 mg/cycle). A maximum error (calculated as the percentage distance between the estimated and the desired total mass, Figure 29) of 10% is achieved when only the magnetization correction is applied, and approximately 5% with both magnetization and pressure wave corrections.

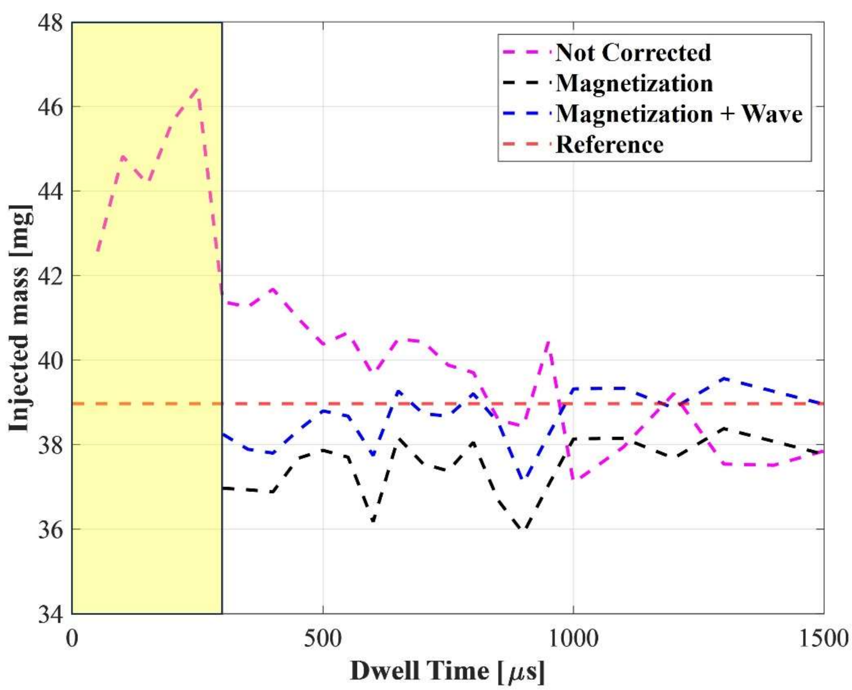

Figure 28: Final compensation for 500 bar with a target total injected mass of 39 mg/cycle of the injected mass with magnetization and pressure wave correction (blue curve), only correction of magnetization (black curve), not corrected consumption (purple curve), reference consumption (red curve) and hydraulic fusion region (in yellow)

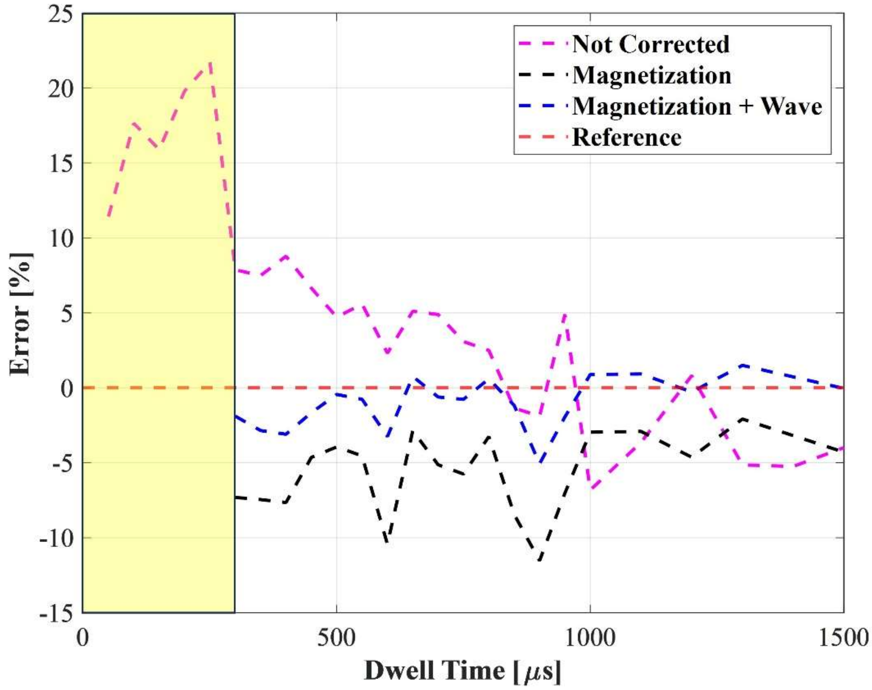

Figure 29: Final compensation error 500 bar with a target total injected mass of 39 mg/cycle of the injected mass with magnetization and pressure wave correction (blue curve), only correction of magnetization (black curve), not corrected consumption (purple curve) and hydraulic fusion region (in yellow)

The obtained results show that the MPW strategy is not only able to properly correct the ET value to compensate for the local pressure reduction within the supply duct and the RM effect at the same time but also capable to damp the mass oscillation (especially visible across DT = 600 μs and DT = 900 μs). In fact, the mean error when only magnetization is corrected is -5.5 % (with an RMSE of 6.1 %) while when both corrections are applied it drops to -0.9 % (with an RMSE of 1.9 %). The presented approach works properly in all the operating points outside the hydraulic fusion region (the study of hydraulic fusion is outside the scope of this paper).

CONCLUSIONS

This paper presents a model-based control strategy to optimize the control of the injected fuel mass when a GDI injector performs multiple injections per cycle. To characterize the system, both electrically and hydraulically, a specially designed open vessel flushing bench was used. A wide experimental campaign was carried out to investigate several operating conditions under single and multiple injection patterns, obtained varying ET, injection pressure and DT.

The analysis of the results obtained in the case of double injections, carried out by changing rail pressure and dwell time, and keeping the duration of the two injections (ET_1 and ET_2) equal and unchanged, showed the high impact of dwell time on the total fuel mass injected. In particular, it was verified that the reduction of dwell time causes an increase in the total injected mass compared to the nominal value (i.e., to that which can be predicted using the injector map). This aspect is mainly related to the residual energy content of the coils of the injector when the second pulse is triggered. The study of this residual magnetization was further investigated by measuring, the excitation current on the coil of the injector. The experimental data showed that the RM makes the current profile of the second injection rise faster during the opening phase, thus leading to an increase in injected mass. To improve the control of the injected mass, the impact of magnetization was modelled (by means of a look-up table capable of representing the effect), and the model was inverted to determine an equivalent ET, function of dwell time between injections and nominal ET of the second injection: this approach can compensate for the distortion of the current profile.

The hydraulic characteristics of the system were also analyzed, mainly based on high-frequency measurements of the instantaneous pressure within the injector supply line. In particular, the pressure fluctuations generated by the first injection were modeled using the mathematical structure of an MSD system. The characteristic parameters of the MSD system were identified (from experimental data) and mapped, as a function of PRail and dwell time, for the two main carriers. The developed model, once calibrated, makes it possible to predict with good accuracy the instantaneous value of the pressure inside the injector feed line without the use of additional sensors (compared to those in the standard engine layout).

Finally, the authors developed a strategy to compensate for the combined effects of residual magnetization and pressure fluctuations at the same time running multiple injections. Specifically, the RM compensation strategy is able to determine an equivalent ET_2 that takes into account the distortion of the current profile, while the instantaneous pressure modeling allows to estimate the real value of pressure upstream of the injector during the second injection, which is normally lower than the pressure in the rail. The proposed approach has been validated in the DT range between the end of the hydraulic fusion region and DT equal to 1500 μs. The presented method, easily implementable in an ECU without the need for supplementary sensors, has been capable to reduce the error on the injected mass to values always lower than 5%.

DATA AVAILABILITY

Data will be available upon reasonable request.

UNCERTAINTIES

This section describes the information about the most important sensors used by the authors during the presented study.

- Pressure wave propagation inside the injector pipes.

Element	Value
Sensor name	Kistler 4067A
Measuring range	0-2000 bar
Overload	500 bar
Sensitivity	5 mV/bar
Linearity	$\leq \pm 0.5$
Natural frequency	> 100 kHz

- Fuel Injected mass.

Element	Value
Sensor name	AVL Balance 733s
Measuring range	0-150 kg/h
Measurement uncertainty	$\leq \pm 0.12$ %
Maximum measurement frequency	10 Hz

- Driving current profiles.

Element	Value
Sensor name	Hioki CT6846A
Rated current	1000 A AC/DC
Frequency bandwidth	DC – 100 kHz
Max allowable input	$\pm$ 1900 Apeak
Accuracy	DC: 0.2 % + 0.02% DC < f < 100 kHz: 0.2% + 0.01%
Linearity	$\pm$ 20 ppm

REFERENCES

[1] Y. Wang, A. Biswas, R. Rodriguez, Z. Keshavarz-Motamed, and A. Emadi, 'Hybrid electric vehicle specific engines: State-of-the-art review', *Energy Rep.*, vol. 8, pp. 832–851, Nov. 2022, doi: 10.1016/j.egyr.2021.11.265.

[2] M. İnci, M. Büyük, M. H. Demir, and G. İlbey, 'A review and research on fuel cell electric vehicles: Topologies, power electronic converters, energy management methods, technical challenges, marketing and future aspects', *Renew. Sustain. Energy Rev.*, vol. 137, p. 110648, Mar. 2021, doi: 10.1016/j.rser.2020.110648.

[3] R. Fu, S. Wang, H. Xu, and Z. Yuan, 'Fuel economy improvement of a turbocharged gasoline SI engine through combining cooled EGR and high compression ratio', *Energy*, vol. 239, p. 122353, Jan. 2022, doi: 10.1016/j.energy.2021.122353.

[4] A. Khameneian *et al.*, 'Dynamic individual-cylinder analysis of a Gasoline Direct Injection engine emissions for cold crank-start at elevated cranking speed conditions of a Hybrid Electric Vehicle', *Control Eng. Pract.*, vol. 129, p. 105349, Dec. 2022, doi: 10.1016/j.conengprac.2022.105349.

[5] A. Solouk, M. Shakiba-Herfeh, J. Arora, and M. Shahbakhti, 'Fuel consumption assessment of an electrified powertrain with a multi-mode high-efficiency engine in various levels of hybridization', *Energy Convers. Manag.*, vol. 155, pp. 100–115, Jan. 2018, doi: 10.1016/j.enconman.2017.10.073.

[6] I. López, E. Ibarra, A. Matallana, J. Andreu, and I. Kortabarria, 'Next generation electric drives for HEV/EV propulsion systems: Technology, trends and challenges', *Renew. Sustain. Energy Rev.*, vol. 114, p. 109336, Oct. 2019, doi: 10.1016/j.rser.2019.109336.

[7] D. Lou *et al.*, 'Investigation of the combustion and particle emission characteristics of a GDI engine with a 50 MPa injection system', *Fuel*, vol. 315, p. 123079, May 2022, doi: 10.1016/j.fuel.2021.123079.

[8] G. Zhu, J. Liu, J. Fu, Z. Xu, Q. Guo, and H. Zhao, 'Experimental study on combustion and emission characteristics of turbocharged gasoline direct injection (GDI) engine under cold start new European driving cycle (NEDC)', *Fuel*, vol. 215, pp. 272–284, Mar. 2018, doi: 10.1016/j.fuel.2017.10.048.

[9] B. Liang *et al.*, 'Comparison of PM emissions from a gasoline direct injected (GDI) vehicle and a port fuel injected (PFI) vehicle measured by electrical low pressure impactor (ELPI) with two fuels: Gasoline and M15 methanol gasoline', *J. Aerosol Sci.*, vol. 57, pp. 22–31, Mar. 2013, doi: 10.1016/j.jaerosci.2012.11.008.

[10] F. Catapano, S. Di Iorio, A. Magno, and B. M. Vaglieco, 'Effect of fuel quality on combustion evolution and particle emissions from PFI and GDI engines fueled with gasoline, ethanol and blend, with focus on 10–23 nm particles', *Energy*, vol. 239, p. 122198, Jan. 2022, doi: 10.1016/j.energy.2021.122198.
[11] P. Dahlander, R. Babayev, S. Ravi Kumar, S. Etikyala, and L. Koopmans, 'Particulates in a GDI Engine and Their Relation to Wall-Film and Mixing Quality', presented at the WCX SAE World Congress Experience, Mar. 2022, pp. 2022-01–0430. doi: 10.4271/2022-01-0430.
[12] C. McCaffery *et al.*, 'On-road gaseous and particulate emissions from GDI vehicles with and without gasoline particulate filters (GPFs) using portable emissions measurement systems (PEMS)', *Sci. Total Environ.*, vol. 710, p. 136366, Mar. 2020, doi: 10.1016/j.scitotenv.2019.136366.
[13] M. M. Maricq, 'Engine, aftertreatment, fuel quality and non-tailpipe achievements to lower gasoline vehicle PM emissions: Literature review and future prospects', *Sci. Total Environ.*, vol. 866, p. 161225, Mar. 2023, doi: 10.1016/j.scitotenv.2022.161225.
[14] A. Yamaguchi, L. Koopmans, A. Helmantel, J. Dillner, and P. Dahlander, 'Spray Behaviors and Gasoline Direct Injection Engine Performance Using Ultrahigh Injection Pressures up to 1500 Bar', *SAE Int. J. Engines*, vol. 15, no. 2, pp. 03-15-01–0007, Jul. 2021, doi: 10.4271/03-15-01-0007.
[15] A. Muddapur, S. Sahu, J. V. Jose, and S. T., 'Spray–wall impingement in a multi-hole GDI injector for split injection at elevated wall temperature and ambient conditions', *Therm. Sci. Eng. Prog.*, vol. 33, p. 101367, Aug. 2022, doi: 10.1016/j.tsep.2022.101367.
[16] M. Costa, U. Sorge, S. Merola, A. Irimescu, M. La Villetta, and V. Rocco, 'Split injection in a homogeneous stratified gasoline direct injection engine for high combustion efficiency and low pollutants emission', *Energy*, vol. 117, pp. 405–415, Dec. 2016, doi: 10.1016/j.energy.2016.03.065.
[17] A. K. Agarwal, V. S. Solanki, and M. Krishnamoorthi, 'Gasoline compression ignition (GCI) combustion in a light-duty engine using double injection strategy', *Appl. Therm. Eng.*, vol. 223, p. 120006, Mar. 2023, doi: 10.1016/j.applthermaleng.2023.120006.
[18] V. Ravaglioli, F. Ponti, G. Silvagni, D. Moro, F. Stola, and M. De Cesare, 'Investigation of Gasoline Partially Premixed Combustion with External Exhaust Gas Recirculation', *SAE Int. J. Engines*, vol. 15, no. 5, pp. 613–629, Dec. 2021, doi: 10.4271/03-15-05-0033.
[19] F. Stola, V. Ravaglioli, G. Silvagni, F. Ponti, and M. De Cesare, 'Injection Pattern Investigation for Gasoline Partially Premixed Combustion Analysis', presented at the 14th International Conference on Engines & Vehicles, Sep. 2019, pp. 2019-24–0112. doi: 10.4271/2019-24-0112.
[20] J. Peng, M. Ma, W. Weizhi, F. Bai, Q. Du, and F. Zhang, 'Characteristics of Rail Pressure Fluctuations under Two-Injection Conditions and the Control Strategy Based on ANN', presented at the International Powertrains, Fuels & Lubricants Meeting, Oct. 2017, pp. 2017-01–2212. doi: 10.4271/2017-01-2212.
[21] A. De Risi, F. Naccarato, and D. Laforgia, 'Experimental Analysis of Common Rail Pressure Wave Effect on Engine Emissions', presented at the SAE 2005 World Congress & Exhibition, Apr. 2005, pp. 2005-01–0373. doi: 10.4271/2005-01-0373.
[22] G. Silvagni *et al.*, 'Development of a Predictive Pressure Waves Model for High-Pressure Common Rail Injection Systems', *SAE Int. J. Engines*, vol. 15, no. 5, pp. 719–741, Dec. 2021, doi: 10.4271/03-15-05-0039.
[23] P. Li, Y. Zhang, T. Li, and L. Xie, 'Elimination of fuel pressure fluctuation and multi-injection fuel mass deviation of high pressure common-rail fuel injection system', *Chin. J. Mech. Eng.*, vol. 28, no. 2, pp. 294–306, Mar. 2015, doi: 10.3901/CJME.2014.1216.180.
[24] A. Cavicchi, L. Postrioti, and E. Scarponi, 'Hydraulic analysis of a GDI injector operation with close multi-injection strategies', *Fuel*, vol. 235, pp. 1114–1122, Jan. 2019, doi: 10.1016/j.fuel.2018.08.089.
[25] D. Viscione *et al.*, 'Experimental characterization of the injected mass variation in a high-pressure GDI injector operating with a multiple injection strategy', *Exp. Charact. Inject. Mass Var. High-Press. GDI Inject. Oper. Mult. Inject. Strategy*, doi: 10.1177/14680874231201263.
[26] '2021-marelli-direct-injection | Automotive News'. Accessed: Oct. 05, 2023. [Online]. Available: https://www.autonews.com/awards/2021-marelli-direct-injection
[27] Y. Wei, L. Fan, Y. Wu, Y. Gu, J. Xu, and H. Fei, 'Research on transmission and coupling characteristics of multi-frequency pressure fluctuation of high pressure common rail fuel system', *Fuel*, vol. 312, p. 122632, Mar. 2022, doi: 10.1016/j.fuel.2021.122632.

[28] H. P. Wang, D. Zheng, and Y. Tian, 'High pressure common rail injection system modeling and control', *ISA Trans.*, vol. 63, pp. 265–273, Jul. 2016, doi: 10.1016/j.isatra.2016.03.002.
[29] M. Corno *et al.*, 'Modelling, Parameter Identification and Dynamics Analysis of a Common Rail Injection System for Gasoline Engines', *IFAC Proc. Vol.*, vol. 41, no. 2, pp. 8481–8486, 2008, doi: 10.3182/20080706-5-KR-1001.01434.
[30] V. K. Gupta, Z. Zhang, and Z. Sun, 'Modeling and control of a novel pressure regulation mechanism for common rail fuel injection systems', *Appl. Math. Model.*, vol. 35, no. 7, pp. 3473–3483, Jul. 2011, doi: 10.1016/j.apm.2011.01.008.
[31] D. Wu, B. Sun, D. Xu, X. An, and Y. Ge, 'Study on Pressure Fluctuation of a Constant Pressure Fuel System', presented at the WCX™ 17: SAE World Congress Experience, Mar. 2017, pp. 2017-01–0828. doi: 10.4271/2017-01-0828.
[32] Y. Ra *et al.*, 'Gasoline DICI Engine Operation in the LTC Regime Using Triple- Pulse Injection', *SAE Int. J. Engines*, vol. 5, no. 3, pp. 1109–1132, Apr. 2012, doi: 10.4271/2012-01-1131.
[33] L. Shi, W. Xiao, M. Li, L. Lou, and K. Deng, 'Research on the effects of injection strategy on LTC combustion based on two-stage fuel injection', *Energy*, vol. 121, pp. 21–31, Feb. 2017, doi: 10.1016/j.energy.2016.12.128.
[34] M. Martínez, C. Altantzis, Y. M. Wright, P. Martí-Aldaraví, and K. Boulouchos, 'Computational study of the Premixed Charge Compression Ignition combustion in a Rapid Compression Expansion Machine: Impact of multiple injection strategy on mixing, ignition and combustion processes', *Fuel*, vol. 318, p. 123388, Jun. 2022, doi: 10.1016/j.fuel.2022.123388.